

# Iterative Convex Optimization for Safety-Critical Model Predictive Control

Shuo Liu<sup>1</sup>, Zhe Huang<sup>1</sup>, Jun Zeng<sup>2</sup>, Koushil Sreenath<sup>2</sup> and Calin A. Belta<sup>3</sup>

**Abstract**—Safety is one of the fundamental challenges in control theory. Recently, multi-step optimal control problems for discrete-time dynamical systems were developed to ensure stability, while adhering to input constraints and safety-critical requirements. This was achieved by incorporating discrete-time Control Barrier Functions (CBFs) within a Model Predictive Control (MPC) framework. Existing work usually centers on the feasibility or safety of optimization problems when the boundaries of safe sets are clearly defined. Most of this research limits discussions to CBFs with relative degree one with respect to the system dynamics. Furthermore, real-time computation becomes challenging in MPC problems with large horizons. In this paper, we introduce a framework that addresses the safety-critical MPC problem through iterative optimization, applicable across CBFs of any relative degree. Our approach involves linearizing the nonlinear system dynamics and safety constraints, modeled as Discrete-time High-Order CBFs (DHOCBFs), at each time step. Additionally, when the boundaries of the safe sets are complex, we present a learning-based method to develop linear boundary equations for these safe sets. These equations are then converted into linearized DHOCBFs. The benefits of computational performance and safe avoidance of obstacles with diverse shapes are examined and confirmed through numerical results.

## I. INTRODUCTION

### A. Motivation

Safety-critical optimal control is a central problem in autonomous systems. For example, reaching a goal while avoiding obstacles and minimizing energy can be formulated as a constrained optimal control problem by using continuous-time Control Barrier Functions (CBFs) [1], [2]. By dividing the timeline into small intervals, the problem is reduced to a (possibly large) number of quadratic programs, which can be solved at real-time speeds. However, this approach may be overly aggressive because it does not anticipate future events.

In [3], the authors use discrete-time CBFs as constraints inside a discrete-time Model Predictive Control (MPC) problem, which provides a safer control policy as it incorporates information about future states over a receding horizon to establish greater safety margins. However, the computational time is relatively large and increases dramatically with

a larger horizon, since the optimization itself is usually nonlinear and non-convex. An additional issue with this nonlinear MPC formulation is the feasibility of the optimization. Moreover, it is difficult to obtain the CBFs from complex environments, i.e., the boundaries of safe sets in the environment are difficult to describe with known equations.

In this article, we address the above challenges by proposing a convex MPC with linearized, discrete-time CBFs, under an iterative approach. In contrast with the real-time iteration (RTI) approach introduced in [4], which solves the problem through iterative Newton steps, our approach solves the optimization problem formulated by a convex MPC iteratively for each time step. If the boundaries of the safe sets are simple and known, we directly linearize these boundaries. If the boundaries of the safe sets are complex, we train a Deep Neural Network (DNN) to obtain linearized boundaries. This DNN is referred to as a Safety Boundary Detector (SBD). The linearized boundaries are then transformed into linearized, discrete-time CBFs to ensure safety.

### B. Related work

1) *Model Predictive Control (MPC)*: This paper can be seen in the context of MPC with safety constraints. MPC is widely used in modern control systems, such as controller design in robotic manipulation and locomotion [5], [6], to obtain a control strategy as a solution to an optimization problem. Stability was achieved in [7] by incorporating Discrete-time Control Lyapunov Functions (DCLFs) into a general MPC-based optimization problem to realize real-time control on a robotic system with limited computational resources. The authors of [8] emphasize safety in robot design and deployment. When safety means obstacle avoidance, some works achieve it through the introduction of repelling functions [1], [9], while others regard obstacle avoidance as one concrete example of safety criteria for robots [10]–[12]. In these works, safety is formulated as constraints in optimization problems.

2) *Control Barrier Functions (CBFs)*: CBFs are used to enforce safety, i.e., rendering a set forward invariant for a dynamical system. Recent studies have demonstrated that to ensure the stabilization of an affine control system, while also adhering to safety constraints and control limitations, CBFs can be integrated with Control Lyapunov Functions (CLFs). This integration facilitates the creation of a sequence of single-step optimization programs [1], [2], [13], [14]. If the cost is quadratic, the optimizations are quadratic programs (QP), and the solutions can be deployed in real time [1], [15]. For safety constraints expressed

This work was supported in part by the NSF under grants IIS-2024606 and CMMI-1944722.

<sup>1</sup>S. Liu and Z. Huang are with Boston University, Brookline, MA, USA {liushuo, huangz7}@bu.edu

<sup>2</sup>J. Zeng and K. Sreenath are with the University of California, Berkeley, CA, 94720, USA {zengjunsjtu, koushils}@berkeley.edu

<sup>3</sup>C. Belta is with the Department of Electrical and Computer Engineering and the Department of Computer Science, University of Maryland, College Park, MD, USA calin@umd.edu

using functions with high relative degree with respect to the dynamics of the system, exponential CBFs [16] and high-order CBFs (HOCBFs) [17]–[19] were proposed. Adaptive, robust, stochastic and feasibility-guaranteed versions of safety-critical control with CBFs were introduced in [20]–[25]. Discrete-time CBFs (DCBFs) were introduced in [26] as a means to enable safety-critical control for discrete-time systems. They were used in a nonlinear MPC (NMPC) framework to create NMPC-DCBF [3], wherein the DCBF constraint was enforced through a predictive horizon. Generalized discrete-time CBFs (GCBFs) and discrete-time high-order CBFs (DHOCBFs) were proposed in [27] and [28] respectively, where the DCBF constraint only acted on the first time-step, i.e., a single-step constraint. MPC with DCBF has been used in various fields, such as autonomous driving [29] and legged robotics [30]. To improve the optimization feasibility, a decay-rate relaxing technique [31] was introduced for NMPC with DCBF [32] for every time-step to simultaneously boost safety and feasibility. However, the overall optimization remains nonlinear and non-convex, resulting in slow processing times for systems with large horizons and nonlinear dynamics (see [32], which is limited to relative-degree one). In this paper, we extend the relaxation techniques introduced in [32] to accommodate high relative-degree CBFs, and largely improve the computational time compared to all existing work.

3) *Learning-Based CBFs*: Many CBF-based methods require explicit equations for the boundaries of the safety sets. When these are not available, they can be learned. In [33], the authors utilized a Support Vector Machine (SVM) to parameterize a CBF. They employed a supervised learning approach to classify regions of the state-space as either safe or unsafe. In [34], the authors proposed a method that incrementally learns a linear CBF by grouping expert demonstrations into linear subspaces and creating low-dimensional representations through fitting. The authors of [35] proposed to construct polynomial CBFs to represent complex obstacles or unreachable regions using logistic regression. However, the above works do not provide theoretical guarantees of correctness of the learned CBFs. The work in [36] proposed and analyzed an optimization-based method for learning a CBF that provides provable safety guarantees given some mild assumptions. Nevertheless, it still requires that the equation of the boundary of the safe set is known. Recently, the authors of [37] defined a learning-based discriminating hyperplane trained on trajectory data from a black-box system to eliminate the dependence on any specific equations for the safe sets. However, the trained hyperplane can only work for that system. In this paper, we train a DNN to construct linear boundaries for obstacles of arbitrary shapes, and the equations of these boundaries can also work as the linearized boundaries of safe sets (linearized DHOCBFs) that can be used by any system.

### C. Contributions

This paper introduces a novel approach to safety-critical MPC that is significantly faster than existing approaches

Acronyms	Meaning
CBF	Control Barrier Function
DCBF	Discrete-Time Control Barrier Function
DHOCBF	Discrete-Time High-Order Control Barrier Function
MPC	Model Predictive Control
NMPC	Nonlinear Model Predictive Control
iMPC	Iterative Model Predictive Control
DNN	Deep Neural Network
SBD	Safety Boundary Detector
CFTOC	Convex Finite-Time Optimal Control
MSE	Mean Squared Error

TABLE I: List of acronyms.

and enhances safety within complex environments where unsafe set boundaries are irregular and poorly defined. The core of our methodology is a learning-based technique for predicting and linearizing the boundaries of safe sets. These predicted boundaries serve as DHOCBFs, facilitating the construction of a sequence of safe operational zones. The key contributions of our work are as follows:

- A method that uses machine learning techniques to accurately predict the linearized boundaries of safe sets. This is particularly effective in scenarios where unsafe set boundaries are complex, irregular, or otherwise difficult to model with traditional equations.
- A model predictive control strategy that ensures safety by enforcing constraints derived from linearized DHOCBFs. We relax these constraints to improve the feasibility of the optimization and to guarantee safety.
- An optimal control framework that integrates linearized system dynamics and DHOCBFs as constraints within a convex optimization problem. This problem is solved iteratively, achieving fast computation speeds ideal for real-time applications.
- Numerical simulations that demonstrate the effectiveness of our framework. A unicycle robot, used as a test case, successfully navigates through narrow spaces populated with both convex and non-convex obstacles, achieving significant improvements in computing speed, safety, and feasibility over existing methods.

This work is a significant extension of our conference paper [38], in which we introduced the idea of linearization of DHOCBFs. In [38], the boundaries of the safe sets were known and simple, e.g., circular. In addition to developing a framework for learning linearized approximation of the boundaries, this manuscript also includes technical details that were omitted in [38], and more complex simulation results.

## II. PRELIMINARIES

In this work, safety is defined as forward invariance of a set  $\mathcal{C}$ , i.e., a system is said to be *safe* if it stays in  $\mathcal{C}$  for all times, given that it is initialized in  $\mathcal{C}$ . We consider the set  $\mathcal{C}$  as the superlevel set of a function  $h : \mathbb{R}^n \rightarrow \mathbb{R}$ :

$$\mathcal{C} := \{\mathbf{x} \in \mathbb{R}^n : h(\mathbf{x}) \geq 0\}. \quad (1)$$

We consider a discrete-time control system in the form

$$\mathbf{x}_{t+1} = f(\mathbf{x}_t, \mathbf{u}_t), \quad (2)$$

where  $\mathbf{x}_t \in \mathcal{X} \subset \mathbb{R}^n$  represents the state of the system at time step  $t \in \mathbb{N}$ ,  $\mathbf{u}_t \in \mathcal{U} \subset \mathbb{R}^q$  is the control input, and the function  $f : \mathbb{R}^n \times \mathbb{R}^q \rightarrow \mathbb{R}^n$  is locally Lipschitz.

**Definition 1** (Relative degree [39]). The output  $y_t = h(\mathbf{x}_t)$  of system (2) is said to have relative degree  $m$  if

$$\begin{aligned} y_{t+i} &= h(\bar{f}_{i-1}(f(\mathbf{x}_t, \mathbf{u}_t))), \quad i \in \{1, 2, \dots, m\}, \\ \text{s.t. } \frac{\partial y_{t+m}}{\partial \mathbf{u}_t} &\neq \mathbf{0}_q, \quad \frac{\partial y_{t+i}}{\partial \mathbf{u}_t} = \mathbf{0}_q, \quad i \in \{1, 2, \dots, m-1\}, \end{aligned} \quad (3)$$

i.e.,  $m$  is the number of steps (delay) in the output  $y_t$  in order for any component of the control input  $\mathbf{u}_t$  to explicitly appear ( $\mathbf{0}_q$  is the zero vector of dimension  $q$ ).

In the above definition, we use  $\bar{f}(\mathbf{x})$  to denote the uncontrolled state dynamics  $f(\mathbf{x}, 0)$ . The subscript  $i$  of function  $\bar{f}(\cdot)$  denotes the  $i$ -times recursive compositions of  $\bar{f}(\cdot)$ , i.e.,  $\bar{f}_i(\mathbf{x}) = \underbrace{\bar{f}(\bar{f}(\dots, \bar{f}(\bar{f}_0(\mathbf{x}))))}_{i\text{-times}}$  with  $\bar{f}_0(\mathbf{x}) = \mathbf{x}$ .

We assume that  $h(\mathbf{x})$  has relative degree  $m$  with respect to system (2) based on Def. 1. Starting with  $\psi_0(\mathbf{x}_t) := h(\mathbf{x}_t)$ , we define a sequence of discrete-time functions  $\psi_i : \mathbb{R}^n \rightarrow \mathbb{R}$ ,  $i = 1, \dots, m$  as:

$$\psi_i(\mathbf{x}_t) := \Delta\psi_{i-1}(\mathbf{x}_t, \mathbf{u}_t) + \alpha_i(\psi_{i-1}(\mathbf{x}_t)), \quad (4)$$

where  $\Delta\psi_{i-1}(\mathbf{x}_t, \mathbf{u}_t) := \psi_{i-1}(\mathbf{x}_{t+1}) - \psi_{i-1}(\mathbf{x}_t)$ , and  $\alpha_i(\cdot)$  denotes the  $i^{\text{th}}$  class  $\kappa$  function which satisfies  $\alpha_i(\psi_{i-1}(\mathbf{x}_t)) \leq \psi_{i-1}(\mathbf{x}_t)$  for  $i = 1, \dots, m$ . A sequence of sets  $\mathcal{C}_i$  is defined based on (4) as

$$\mathcal{C}_i := \{\mathbf{x} \in \mathbb{R}^n : \psi_i(\mathbf{x}) \geq 0\}, \quad i \in \{0, \dots, m-1\}. \quad (5)$$

**Definition 2** (DHOCBF [28]). Let  $\psi_i(\mathbf{x})$ ,  $i \in \{1, \dots, m\}$  be defined by (4) and  $\mathcal{C}_i$ ,  $i \in \{0, \dots, m-1\}$  be defined by (5). A function  $h : \mathbb{R}^n \rightarrow \mathbb{R}$  is a Discrete-time High-Order Control Barrier Function (DHOCBF) with relative degree  $m$  for system (2) if there exist  $\psi_m(\mathbf{x})$  and  $\mathcal{C}_i$  such that

$$\psi_m(\mathbf{x}_t) \geq 0, \quad \forall \mathbf{x}_t \in \mathcal{C}_0 \cap \dots \cap \mathcal{C}_{m-1}, t \in \mathbb{N}. \quad (6)$$

**Theorem 1** (Safety Guarantee [28]). *Given a DHOCBF  $h(\mathbf{x})$  from Def. 2 with corresponding sets  $\mathcal{C}_0, \dots, \mathcal{C}_{m-1}$  defined by (5), if  $\mathbf{x}_0 \in \mathcal{C}_0 \cap \dots \cap \mathcal{C}_{m-1}$ , then any Lipschitz controller  $\mathbf{u}_t$  that satisfies the constraint in (6),  $\forall t \geq 0$  renders  $\mathcal{C}_0 \cap \dots \cap \mathcal{C}_{m-1}$  forward invariant for system (2), i.e.,  $\mathbf{x}_t \in \mathcal{C}_0 \cap \dots \cap \mathcal{C}_{m-1}, \forall t \geq 0$ .*

**Remark 1.** *The function  $\psi_i(\mathbf{x})$  in (4) is called an  $i^{\text{th}}$  order Discrete-time Control Barrier Function (DCBF) in this paper. If the constraints in an optimal control problem include only DCBF constraints ( $\psi_i(\mathbf{x}_t) \geq 0$ ), we must formulate the DCBF constraints up to the  $m^{\text{th}}$  order to ensure that the control input  $\mathbf{u}_t$  is explicitly represented based on Def. 1. However, if the constraints also include the system constraint (2), where the control input  $\mathbf{u}_t$  is already explicitly represented, we can flexibly select a suitable order for the DCBF constraints to minimize computational demands. In other words, the highest order for DCBF could be  $m_{\text{cbf}}$  with*

$m_{\text{cbf}} \leq m$ . We can simply define an  $i^{\text{th}}$  order DCBF  $\psi_i(\mathbf{x})$  in (4) as

$$\psi_i(\mathbf{x}_t) := \Delta\psi_{i-1}(\mathbf{x}_t, \mathbf{u}_t) + \gamma_i\psi_{i-1}(\mathbf{x}_t), \quad (7)$$

where  $\alpha(\cdot)$  is defined linear and  $0 < \gamma_i \leq 1, i \in \{1, \dots, m_{\text{cbf}}\}$ .

The expression presented in (7) adheres to the structure of the first-order DCBF introduced in [26] and can be applied to define a DHOCBF with any relative degree for the classical constrained, safety-critical optimal control problem:

$$\mathbf{u}_t^* = \underset{\mathbf{u}_t}{\operatorname{argmin}} \mathbf{u}_t^T \mathbf{u}_t + \sum_{k=t}^{t+1} (\mathbf{x}_k - \mathbf{x}_e)^T (\mathbf{x}_k - \mathbf{x}_e) \quad (8a)$$

$$\text{s.t. } \mathbf{x}_{t+1} = f(\mathbf{x}_t, \mathbf{u}_t), \quad (8b)$$

$$\psi_{i-1}(\mathbf{x}_{t+1}) \geq (1 - \gamma_i)\psi_{i-1}(\mathbf{x}_t), \quad 0 < \gamma_i \leq 1, \quad (8c)$$

$$\mathbf{u}_t \in \mathcal{U} \subset \mathbb{R}^q, \quad \mathbf{x}_t \in \mathcal{X} \subset \mathbb{R}^n, \quad (8d)$$

where  $\mathbf{x}_e$  denotes a reference state,  $0 \leq t \leq T, t \in \mathbb{N}$  and the function  $\psi_{i-1}, i \in \{1, \dots, m_{\text{cbf}}\}$  in (8c) ensures that the state  $\mathbf{x}_t$  of system (8b) stays within a safe set  $\mathcal{C}$  according to (1). The constraint (8d) bounds the control input and state, which may conflict with constraint (8b) and (8c), leading to infeasibility. Note that solving the problem described above can only yield the current optimal control input, resulting in a greedy control policy that considers short-term (one-step) safety and may overlook safer solutions. Furthermore, there is a trade-off between safety performance and feasibility. As discussed in [3], both safety and feasibility cannot be enhanced simultaneously. In [3], the authors show that MPC with DCBFs can give a safer control policy, as it takes future state and control information into account. A version of nonlinear MPC that incorporates DCBFs (called NMPC-DCBF) with a relaxation technique and simultaneously enhances feasibility and safety was developed in [32]. This approach, although it can flexibly incorporate the system's physical constraints and safety requirements as soft or hard constraints into the control strategy, often leads to non-convex optimization problems, resulting in inherently high computational complexity. In this paper, we show how to linearize the system and DCBF constraints to obtain a convex finite-time optimal control (CFTOC) framework within an MPC setting, which significantly improves computational efficiency.

### III. PROBLEM FORMULATION AND APPROACH

Our objective is to find a closed-loop control strategy for system (2) over a time interval  $[0, T]$  that minimizes the deviation from a reference state, complies with safety requirements, and satisfies constraints on states and control inputs.

**Safety Requirement:** System (2) should always satisfy a safety requirement of the form:

$$h(\mathbf{x}_t) \geq 0, \quad \mathbf{x}_t \in \mathbb{R}^n, \quad 0 \leq t \leq T, \quad (9)$$

where  $h : \mathbb{R}^n \rightarrow \mathbb{R}$ .

**Control and State Limitation Requirements:** The controller  $\mathbf{u}_t$  and state  $\mathbf{x}_t$  must satisfy (8d) for  $0 \leq t \leq T$ .

**Objective:** We consider the following cost over a receding horizon  $N < T$ :

$$J(\mathbf{u}_{t,k}) = \sum_{k=0}^{N-1} \mathbf{u}_{t,k}^T \mathbf{u}_{t,k} + \sum_{k=0}^N (\mathbf{x}_{t,k} - \mathbf{x}_e)^T (\mathbf{x}_{t,k} - \mathbf{x}_e), \quad (10)$$

where  $\mathbf{x}_{t,k}$ ,  $\mathbf{u}_{t,k}$  are the state and input predictions (according to the system's dynamics) at time  $t+k$  made at the current time  $t$ ,  $0 \leq t \leq T$ . We denote  $\mathbf{x}_{t,0} = \mathbf{x}_t$ ,  $\mathbf{u}_{t,0} = \mathbf{u}_t$  and the reference state as  $\mathbf{x}_e$ . A control policy is *feasible* if all the constraints guaranteeing the aforementioned requirements are mutually non-conflicting for all  $0 \leq t \leq T$ . In this paper, we consider the following problem:

**Problem 1.** Find a feasible control policy for system (2) such that the safety and the control and state limitations requirements are satisfied and cost (10) is minimized.

As mentioned at the end of Sec. II, to satisfy the safety requirement, the authors of [32] incorporated the DCBF constraint

$$h(\mathbf{x}_{t,k+1}) \geq \omega_{t,k}(1-\gamma)h(\mathbf{x}_{t,k}), \quad 0 < \gamma \leq 1 \quad (11)$$

into MPC with a relaxation variable  $\omega_{t,k} \in \mathbb{R}$ , which simultaneously enhances feasibility and safety. They also formulated (2) and (8d) as constraints in the MPC to meet additional requirements, which results in the entire optimization problem being nonconvex, as (11) and (2) are often nonlinear. This method, referred to as NMPC-DCBF, can lead to slow processing times for systems with large horizons. Another issue is that, when the boundary of the unsafe set is difficult to express with explicit equations, it becomes challenging to obtain a DCBF candidate  $h(\mathbf{x})$ . Some approaches [3], [40] exist for the case when the boundaries of the unsafe sets are circular or polytopic. In many real-world situations, this assumption is restrictive. Meanwhile, using a known unsafe set to replace the original unsafe set often results in a safe set that is much smaller than the original safe set (see e.g., [40], where the authors used NMPC to ensure safe path following for a unicycle robot). However, due to the presence of numerous polytopic obstacles in the map, defining the safe region using linear equations corresponding to the edges of the polytopes results in a very small safe region. This forced the authors to consider only obstacles within a certain distance, making it difficult for the NMPC to effectively handle obstacles beyond that range.

To improve the computational efficiency of solving the optimization problem and obtain a DHOCBF candidate  $h(\mathbf{x})$  from a complex unsafe set, our approach to Problem 1 proceeds as follows. We design the Safety Boundary Detector (SBD) to get the linearized boundaries of unsafe sets. If the boundaries of unsafe sets are simple and known, SBD can directly linearize these boundaries. If they are complex or unknown, SBD relies on a trained Deep Neural Network (DNN) to predict linearized boundaries of unsafe sets. The equation

of every linearized boundary can be used as a DHOCBF candidate  $h(\mathbf{x})$  to construct the corresponding linearized DHOCBF constraint. Since at each time step, an unsafe set corresponds to only one DHOCBF constraint (unlike in [40], where an unsafe set corresponds to multiple DCBF constraints), the coverage of the safe set is large (the safe set is constructed by the intersection of DHOCBF constraints). We present a MPC framework, where the safety requirement is enforced by linearized DHOCBF constraints, and the constraints on states and control inputs are incorporated. Each DHOCBF constraint is relaxed to enhance feasibility. Additionally, the constraint corresponding to the system dynamics is linearized. This optimal control framework is a fast-computing convex optimization designed to be solved iteratively, ensuring that the error in decision variables is minimized after a certain number of iterations.

#### IV. ITERATIVE CONVEX MPC WITH DHOCBF

In this section, we present an iterative convex MPC for general DHOCBFs defined in Sec. II.

##### A. Iterative Convex MPC

Our proposed approach, which is depicted in Fig. 1, involves iterative optimizations at each time step  $t$ , which is denoted as *iterative* MPC-DHOCBF (iMPC-DHOCBF). Our iterative optimization problem contains three parts for each iteration  $j$ : (1) solving a CFTOC problem with linearized dynamics and DHOCBF to get optimal values of states and inputs  $\mathbf{X}_t^{*,j} = [\mathbf{x}_{t,0}^{*,j}, \dots, \mathbf{x}_{t,N}^{*,j}]$ ,  $\mathbf{U}_t^{*,j} = [\mathbf{u}_{t,0}^{*,j}, \dots, \mathbf{u}_{t,N-1}^{*,j}]$ , (2) checking convergence, (3) updating the state and input vectors for next iteration, i.e.,  $\bar{\mathbf{X}}_t^{j+1} = \mathbf{X}_t^{*,j}$ ,  $\bar{\mathbf{U}}_t^{j+1} = \mathbf{U}_t^{*,j}$ . Notice that the open-loop trajectory with updated states  $\bar{\mathbf{X}}_t^j = [\bar{\mathbf{x}}_{t,0}^j, \dots, \bar{\mathbf{x}}_{t,N-1}^j]$  and inputs  $\bar{\mathbf{U}}_t^j = [\bar{\mathbf{u}}_{t,0}^j, \dots, \bar{\mathbf{u}}_{t,N-1}^j]$  is passed between iterations, which allows iterative linearization for both system dynamics and DHOCBF locally.

The iteration is finished when the convergence error function  $e(\mathbf{X}_t^{*,j}, \mathbf{U}_t^{*,j}, \bar{\mathbf{X}}_t^j, \bar{\mathbf{U}}_t^j)$  is within a user-defined normalized convergence criterion. To restrict the number of iterations, we limit  $j < j_{\max}$ , where  $j_{\max}$  denotes the maximum numbers of iterations. Therefore, the iterative optimization process halts upon reaching a local minimum for the cost function, meeting the convergence criterion, or when the iteration count equals  $j_{\max}$ . The optimized states  $\mathbf{X}_t^*$  and inputs  $\mathbf{U}_t^*$  from the last iteration are passed to the iMPC-DHOCBF for the next time instant as  $\bar{\mathbf{U}}_{t+1}^0, \bar{\mathbf{X}}_{t+1}^0$ . At each time step, we record the updated states  $\mathbf{x}_{t+1}$  propagated by the system dynamics  $\mathbf{x}_{t+1} = f(\mathbf{x}_t, \mathbf{u}_{t,0}^*)$ , enabling us to extract a closed-loop trajectory. Note that if we have the boundaries of unsafe sets, the SBD can directly linearize safe boundaries by finding the point nearest to the system and drawing a tangent surface at that point. If we do not have the boundaries of unsafe sets, SBD relies on a DNN that is trained before the start of the iMPC. The advantage of this approach is that we have pre-trained a DNN which can learn in advance information about all unsafe sets in the environment, especially when the boundaries of the unsafe sets cannot be accurately identified and described. Consequently,

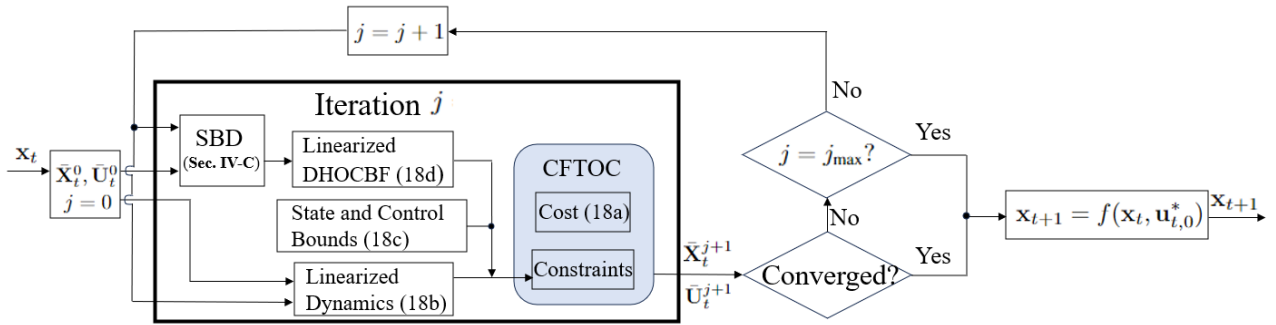


Fig. 1: Schematic of the iterative process of solving the convex MPC at time  $t$ . The safety boundary detector (SBD) generates linearized boundaries for unsafe sets, which are transformed to linearized DHOCBFs. At each iteration, we solve a convex finite-time optimal control (CFTOC) problem with linearized dynamics and DHOCBF. The cost is quadratic with a positive semidefinite weight matrix and the constraints are linear, which makes the CFTOC problem a convex optimization. After each iteration, a convergence criterion is checked to decide whether to proceed to the next iteration or update the state  $\mathbf{x}_{t+1}$ .

the time required to perform inference with this DNN for obtaining the linearized DHOCBF is essentially fixed in each iteration and can gradually decrease as adjustments are made to the DNN, ensuring the efficiency of solving each CFTOC.

**Remark 2 (Warm Start).** At  $t = 0$ , the initial guess for the control input in the leftmost block in Fig. 1 is  $\bar{\mathbf{U}}_0^0 = 0$ , based on which we get the initial nominal state  $\bar{\mathbf{X}}_0^0$ . This initial guess could make the optimization infeasible if the nominal state lies within the infeasible set. A good initial guess is still needed for faster numerical convergence.

### B. Linearization of Dynamics

At iteration  $j$ , a control vector  $\mathbf{u}_{t,k}^j$  is obtained by linearizing the system around  $\bar{\mathbf{x}}_{t,k}^j, \bar{\mathbf{u}}_{t,k}^j$ :

$$\mathbf{x}_{t,k+1}^j - \bar{\mathbf{x}}_{t,k+1}^j = A^j (\mathbf{x}_{t,k}^j - \bar{\mathbf{x}}_{t,k}^j) + B^j (\mathbf{u}_{t,k}^j - \bar{\mathbf{u}}_{t,k}^j), \quad (12)$$

where  $0 \leq j < j_{\max}$ ;  $k$  and  $j$  represent open-loop time step and iteration indices, respectively. We also have

$$A^j = D_{\mathbf{x}} f(\bar{\mathbf{x}}_{t,k}^j, \bar{\mathbf{u}}_{t,k}^j), \quad B^j = D_{\mathbf{u}} f(\bar{\mathbf{x}}_{t,k}^j, \bar{\mathbf{u}}_{t,k}^j), \quad (13)$$

where  $D_{\mathbf{x}}$  and  $D_{\mathbf{u}}$  denote the Jacobian of the system dynamics  $f(\mathbf{x}, \mathbf{u})$  with respect to the state  $\mathbf{x}$  and the input  $\mathbf{u}$ . This approach allows us to linearize the system at  $(\bar{\mathbf{x}}_{t,k}^j, \bar{\mathbf{u}}_{t,k}^j)$  locally between iterations. The convex system dynamics constraints are provided in (12) since all the nominal vectors  $(\bar{\mathbf{x}}_{t,k}^j, \bar{\mathbf{u}}_{t,k}^j)$  at the current iteration are constant and constructed from the previous iteration  $j - 1$ .

### C. Linearized SBD-Generated DCBF and DHOCBF

1) *Safety Boundary Detector for Known Unsafe Boundaries:* In this section, we show how to linearize the DCBF up to the highest order with known unsafe boundary  $h(\mathbf{x}) = 0$ . At iteration  $j$  and time step  $t + k$ , as shown in Fig. 2, in order to linearize  $h(\mathbf{x}_{t,k}^j)$ , an explicit dashed line is projected in the state space to the nearest point  $\tilde{\mathbf{x}}_{t,k}^j$  on the boundary of the unsafe set from each state  $\bar{\mathbf{x}}_{t,k}^j$ . Note that  $\bar{\mathbf{x}}_{t,k}^j$  is the nominal state vector from iteration  $j - 1$  for the linearization at iteration  $j$ , which means  $\bar{\mathbf{x}}_{t,k}^j = \mathbf{x}_{t,k}^{j-1}$ . The solid line perpendicular to the dashed line passing through

the nearest point  $\tilde{\mathbf{x}}_{t,k}^j$  is denoted as  $h_{\parallel}(\mathbf{x}_{t,k}^j, \tilde{\mathbf{x}}_{t,k}^j)$ . This allows us to incorporate the above process into the SBD to define a linearized safe set by  $h_{\parallel}(\mathbf{x}_{t,k}^j, \tilde{\mathbf{x}}_{t,k}^j) \geq 0, \forall t \in \mathbb{N}$  by the green region. Note that  $\tilde{\mathbf{x}}_{t,k}^j$  generally represents the optimized value of the minimum distance problem with distance function  $h(\cdot)$  between  $\bar{\mathbf{x}}_{t,k}^j$  and safe set  $\mathcal{C}$ . Since  $h(\cdot)$  is known and continuous, for common shapes of unsafe sets, the expression of  $\tilde{\mathbf{x}}_{t,k}^j$  as a function of  $\bar{\mathbf{x}}_{t,k}^j$  is explicit. For example, when  $h(\cdot)$  describes a  $l_2$ -norm function with the unsafe set being a circular shape,  $\tilde{\mathbf{x}}_{t,k}^j$  is exactly the intersection point of the line determined by  $\bar{\mathbf{x}}_{t,k}^j$  and the center of the circular region with the circumference.

The relative degree of  $h_{\parallel}(\mathbf{x}_{t,k}^j, \tilde{\mathbf{x}}_{t,k}^j)$  with respect to system (2) is still  $m$  when the relative degree of  $h(\mathbf{x}_{t,k}^j)$  is  $m$ . Thus, in order to guarantee safety with forward invariance based on Thm. 1 and Rem. 1, two sufficient conditions need to be satisfied: (1) the sequence of linearized DHOCBF  $\tilde{\psi}_0(\cdot), \dots, \tilde{\psi}_{m_{\text{cbf}}-1}(\cdot)$  is larger or equal to zero at the initial condition  $\mathbf{x}_t$ , and (2) the highest-order DCBF constraint  $\tilde{\psi}_{m_{\text{cbf}}}(\mathbf{x}) \geq 0$  is always satisfied, where  $\tilde{\psi}_i(\cdot)$  is defined as:

$$\begin{aligned} \tilde{\psi}_0(\mathbf{x}_{t,k}^j) &:= h_{\parallel}(\mathbf{x}_{t,k}^j, \tilde{\mathbf{x}}_{t,k}^j) \\ \tilde{\psi}_i(\mathbf{x}_{t,k}^j) &:= \tilde{\psi}_{i-1}(\mathbf{x}_{t,k+1}^j) - \tilde{\psi}_{i-1}(\mathbf{x}_{t,k}^j) + \gamma_i \tilde{\psi}_{i-1}(\mathbf{x}_{t,k}^j). \end{aligned} \quad (14)$$

Here, we have  $0 < \gamma_i \leq 1, i \in \{1, \dots, m_{\text{cbf}}\}$ , and  $m_{\text{cbf}} \leq m$  (as in (7)). From Rem. 1, it follows that  $m_{\text{cbf}}$  is not necessarily equal to  $m$ . A detailed discussion on this can be found in [27], [32].

An important issue is *feasibility*. It is possible that  $\tilde{\psi}_i(\mathbf{x}_{t,k}^j) \geq 0, 1 \leq i \leq m_{\text{cbf}} - 1$ , with  $k \in \{0, \dots, N\}$  is not satisfied since the linearized DHOCBF functions  $\tilde{\psi}_0(\cdot), \dots, \tilde{\psi}_{m_{\text{cbf}}-1}(\cdot)$  are more conservative than the original forms  $\psi_0(\cdot), \dots, \psi_{m_{\text{cbf}}-1}(\cdot)$ . This problem can occur when the horizon is too large, or the linearization is too conservative. In order to handle this issue, we introduce a slack variable  $\omega_{t,k,i}^j$  with a corresponding decay rate  $(1 - \gamma_i)$ :

$$\tilde{\psi}_{i-1}(\mathbf{x}_{t,k+1}^j) \geq \omega_{t,k,i}^j (1 - \gamma_i) \tilde{\psi}_{i-1}(\mathbf{x}_{t,k}^j), \quad \omega_{t,k,i}^j \in \mathbb{R}, \quad (15)$$

where  $i \in \{1, \dots, m_{\text{cbf}}\}$ . The slack variable  $\omega_{t,k,i}^j$  is selected by minimizing a cost function term to satisfy DCBF

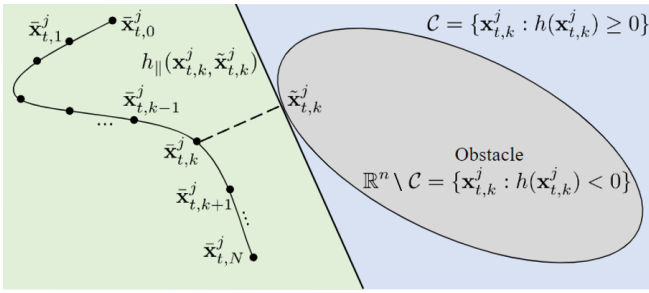


Fig. 2: Linearization of DHOCBF:  $h_{\parallel}(\mathbf{x}_{t,k}^j, \tilde{\mathbf{x}}_{t,k}^j) \geq 0$  represents the linearized safe set locally and is colored in green. Note that  $h_{\parallel}(\mathbf{x}_{t,k}^j, \tilde{\mathbf{x}}_{t,k}^j) \geq 0$  guarantees  $h(\mathbf{x}_{t,k}^j) \geq 0$  (colored in blue plus green), which ensures collision avoidance (outside the grey region).

constraints at initial condition at any time step [32].

Another challenge stemming from the linearization of the DCBF is that the constraints in (15) might become non-convex, e.g., if  $i = k = 1$ , Eqn. (15) becomes a nonconvex inequality:

$$\tilde{\psi}_0(\mathbf{x}_{t,2}^j) \geq \omega_{t,1,1}^j (1 - \gamma_1) \tilde{\psi}_0(\mathbf{x}_{t,1}^j), \quad \omega_{t,1,1}^j \in \mathbb{R}, \quad (16)$$

where both  $\omega_{t,1,1}^j$  and  $\mathbf{x}_{t,1}^j$  are optimization variables. It is important to note that  $\tilde{\psi}_0(\mathbf{x}_{t,0}^j)$  is always constant; therefore, we can position  $\omega_{t,1,1}^j$  in front of  $\tilde{\psi}_0(\mathbf{x}_{t,0}^j)$  and relocate the other optimization variables to the opposite side of the inequalities. Eqn. (16) can be rewritten as

$$\tilde{\psi}_0(\mathbf{x}_{t,2}^j) \geq \omega_{t,1,1}^j (1 - \gamma_1)^2 \tilde{\psi}_0(\mathbf{x}_{t,0}^j), \quad \omega_{t,1,1}^j \in \mathbb{R}, \quad (17)$$

which is linear and convex. This motivates us to propose the following form that replaces (15) as a convex constraint:

$$\begin{aligned} \tilde{\psi}_{i-1}(\mathbf{x}_{t,k}^j) + \sum_{\nu=1}^i Z_{\nu,i} (1 - \gamma_i)^k \tilde{\psi}_0(\mathbf{x}_{t,\nu}^j) &\geq \\ \omega_{t,k,i}^j Z_{0,i} (1 - \gamma_i)^k \tilde{\psi}_0(\mathbf{x}_{t,0}^j), & \\ j \leq j_{\max} \in \mathbb{N}^+, i \in \{1, \dots, m_{\text{cbf}}\}, \omega_{t,k,i}^j &\in \mathbb{R}. \end{aligned} \quad (18)$$

In the above,  $Z_{\nu,i}$  is a constant that can be obtained recursively by reformulating  $\tilde{\psi}_{i-1}(\cdot)$  back to  $\tilde{\psi}_0(\cdot)$  given  $\nu \in \{0, \dots, i\}$ . We define  $Z_{\nu,i}$  as follows. When  $2 \leq i, \nu \leq i - 2$ , we have

$$\begin{aligned} Z_{\nu,i} &= \sum_{l=1}^{l_{\max}} [(\gamma_{\zeta_1} - 1)(\gamma_{\zeta_2} - 1) \cdots (\gamma_{\zeta_{i-\nu-1}} - 1)] l, \\ \zeta_1 &< \zeta_2 < \cdots < \zeta_{i-\nu-1}, \zeta_s \in \{1, 2, \dots, i - 1\}, \end{aligned} \quad (19)$$

where  $l_{\max} = \binom{i-1}{i-\nu-1}$ ,  $\zeta_s$  denotes  $\zeta_1, \zeta_2, \dots, \zeta_{i-\nu-1}$ .  $[\cdot]l$  denotes the  $l^{\text{th}}$  combination of the product of the elements in parenthesis, e.g., if  $i = 4, \nu = 1$ ,  $Z_{1,4} = (\gamma_1 - 1)(\gamma_2 - 1) + (\gamma_1 - 1)(\gamma_3 - 1) + (\gamma_2 - 1)(\gamma_3 - 1)$ . For the case  $\nu = i - 1$ , if  $2 \leq i$ , we define  $Z_{\nu,i} = -1$ ; if  $i = 1$ , we define  $Z_{\nu,i} = 1$ . Besides that, we define  $Z_{\nu,i} = 0$  for the case  $\nu = i$  (Eqn. (17) shows the case where  $Z_{0,1} = 1, Z_{1,1} = 0$ ).

**Remark 3.** Note that if we position  $\omega_{t,k,i}^j$  in front of  $\sum_{\nu=1}^i Z_{\nu,i} (1 - \gamma_i)^k \tilde{\psi}_0(\mathbf{x}_{t,\nu}^j)$  in (18), Eqn. (15) is the same as (18). This illustrates that the decay rate in (18) used by

the iMPC-DHOCBF is partially relaxed compared to the one in (15) due to the requirement of the linearization. This can affect the feasibility of the optimization.

2) *Safety Boundary Detector for Unknown Unsafe Boundaries:* Notice that  $\tilde{\mathbf{x}}_{t,k}^j$  in Sec. IV-C.1 could be implicit if  $h(\cdot)$  is unknown or discontinuous, or for unsafe sets of irregular shapes (like general ellipse), but it could still be numerically approximated as the values of  $\tilde{\mathbf{x}}_{t,k}^j$  known at iteration  $j$  before the linearization, i.e., if we could predict the nearest point  $\tilde{\mathbf{x}}_{t,k}^j$  for the  $i^{\text{th}}$  unsafe set. For a map, the linearized unsafe set can be expressed as

$$h_{\parallel}(\mathbf{x}_{t,k}^j, \tilde{\mathbf{x}}_{t,k}^j) = (\tilde{\mathbf{x}}_{t,k}^j - \bar{\mathbf{x}}_{t,k}^j)^T (\mathbf{x}_{t,k}^j - \tilde{\mathbf{x}}_{t,k}^j), \quad (20)$$

which can also be used as a linearized DHOCBF in Sec. IV-C.1. Specifically, it involves finding the nearest point on the boundary of an unsafe set or an inaccessible region relative to the current position, and then constructing a tangent line or plane through that point to serve as the linearized unsafe boundary. Next we will show how to design a Deep Neural Network (DNN) to get the approximate nearest point  $\tilde{\mathbf{x}}_{t,k}^j$ .

The designed DNN learns and memorizes a specific map to identify and return the nearest point on each unsafe set relative to the system. A line perpendicular to the connection between the system and the nearest point serves as the linearized boundary for the corresponding unsafe set. During training data acquisition, nearest points on unsafe sets are collected for every safe point on the map as ground truth, which the DNN learns through supervised training, reflecting its memory capacity. To efficiently memorize training data, we focus on networks with strong associative memory capabilities, as conventional DNNs excel at pattern recognition but are not naturally suited for memory registers. However, certain neural network architectures are better designed for this purpose. Several research studies and models, such as Hopfield Networks, Neural Turing Machines, Autoencoders [41], and Transformers, are particularly relevant to this task.

**Model Selection:** We use an Autoencoder framework for its efficiency in encoding complex patterns, but to streamline the model and enhance inference speed, we utilize only the encoder. This approach focuses on efficient information retrieval rather than input reconstruction.

During training, the encoder compresses the map into a lower-dimensional space by minimizing the loss between predicted nearest points and the ground truth, capturing essential map information. Once trained, it effectively recalls the nearest points on boundaries, acting as a memory register.

We omit the decoder since input reconstruction isn't required; our priority is quick information access. The encoder maintains consistent inference times by processing inputs into a condensed representation, unaffected by the map's complexity (e.g., the number of unsafe sets), ensuring efficient and predictable performance.

**Map Processing:** We start by identifying the boundaries of unsafe sets on a pixel-based canvas that mimics real-world convex and non-convex shapes. Without precise mathematical descriptions, we use digital image processing techniques

to detect and highlight the pixels along the boundaries of these shapes.

After identifying the boundaries, we avoid using every boundary pixel to maintain efficiency. Instead, we select a subset of these pixels, creating a discrete contour for each shape. These discrete points effectively represent the unsafe sets on any map. For each new map, the same method accurately outlines the contours of unsafe sets, regardless of their shapes. The processed pixel-based boundaries of unsafe sets are displayed in the map of Fig. 3.  $[x, y]^T$  denotes the current location of system, and  $[x_1, y_1, \dots, x_p, y_p]^T$  represent the nearest points on each boundary to the system, obtained by comparing each pixel. Both system's location and nearest point are depicted by red dots.

**Network Design and Training:** As described above, we employ the encoder part of a neural network known as an Autoencoder. Fig. 3 illustrates the structure of our network, which starts with multiple layers having a high number of nodes (high feature dimensions) to capture detailed environmental data. This number decreases as the data progresses through subsequent layers. This design focuses on extracting essential information from the map. Each layer is fully connected to the next, ensuring comprehensive processing and integration of all memorized aspects of the environmental data. Specifically, the network's input takes a pair of numbers  $[x, y]^T$  representing the current location of system, while the output delivers coordinates  $[\tilde{x}_1, \tilde{y}_1, \dots, \tilde{x}_p, \tilde{y}_p]^T$  for the predicted nearest points on nearby unsafe sets. When adapting to various maps, the output size of our network varies depending on the number of unsafe sets in each map. This variation may necessitate re-training the network to acquaint it with the changes in the environment.

The first hidden layer is denoted as  $h_0$ . The subsequent layers' dimensions are defined by:

$$h_i = h_0 - i * \text{floor}((h_0 - l_{out})/L), \quad (21)$$

in which  $h_i$  stands for the number of nodes in the  $i^{\text{th}}$  of hidden layers,  $l_{out}$  is the output layer size, and  $L$  denotes the total number of hidden layers. The floor function rounds down a real number to the nearest integer less than or equal to that number. This model architecture, which uniformly reduces layer by layer, can adaptively adjust to the size of the output and ensure smoothness in dimension reduction.

To train the network, we collect sampled system locations within the map and identify the nearest points on the unsafe set boundaries as ground truth. When multiple nearest points exist (common with nonconvex boundaries), we arbitrarily select one. Sampled locations can be inside or outside the unsafe sets, enhancing the network's ability to identify the nearest boundary points. The data (sampled locations and ground truths) is split into a training set and a testing set. The training set is used for network training, while the testing set (with sampled locations outside the unsafe sets) evaluates the network's accuracy in predicting the nearest points relative to the system. Since the network's output  $[\tilde{x}_i, \tilde{y}_i]^T, i \in \{1, \dots, p\}$  could be used as the approximate nearest points, we can incorporate the above process into the SBD to

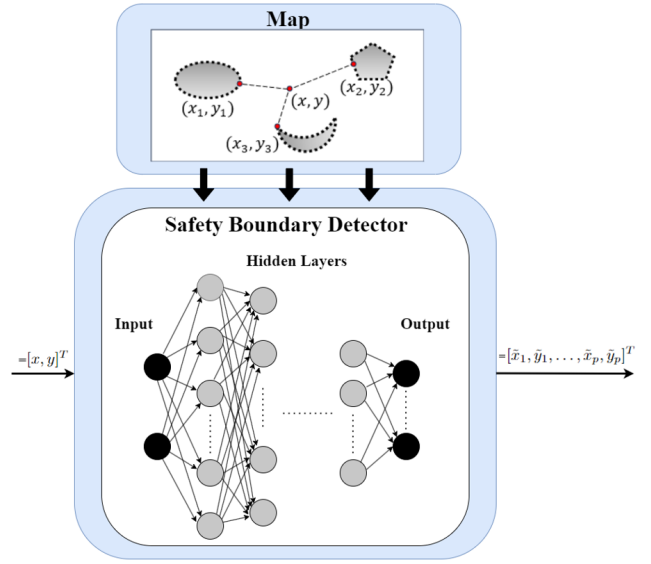


Fig. 3: System identification for the safety boundary detector, which is a DNN trained with data from a map. The input of SBD is the current location of system  $(x, y)$ , and the output is the nearest point  $(\tilde{x}_i, \tilde{y}_i)$  on the boundary of each of the  $p$  unsafe sets relative to the system, with one nearest point corresponding to each set.

define linearized safe sets from (20) by  $h_{\parallel}(\mathbf{x}_{t,k}^j, \tilde{\mathbf{x}}_{t,k}^j) \geq 0$ ,  $\forall t \in \mathbb{N}$  similar to Fig. 2. The linearization of the DHOCBF  $h_{\parallel}(\mathbf{x}_{t,k}^j, \tilde{\mathbf{x}}_{t,k}^j)$  up to the highest order will be the same as shown in Sec. IV-C.1.

**Remark 4 (Continuity of  $h_{\parallel}(\cdot)$ ).** Whether the equation of a linearized safe boundary (20) to a continuous boundary is continuous with respect to point  $\mathbf{x}_{t,k}^j$  depends on the properties and smoothness of the curve. For smooth boundaries, such as circles or ellipses, the nearest point  $\tilde{\mathbf{x}}_{t,k}^j$  to an external point  $\mathbf{x}_{t,k}^j$  can typically be calculated, and this point changes continuously as  $\mathbf{x}_{t,k}^j$  moves. In these cases, (20) is usually continuous as well. However, for shapes with sharp corners or discontinuities, like stars, the location of the nearest point may jump abruptly with minor movements of  $\mathbf{x}_{t,k}^j$  (jumping from one vertex to another or from an edge to a vertex), leading to discontinuities in Eqn. (20) at these points. The pixel-based boundary approximation introduced in Sec. IV-C.2 will also bring discontinuity. Discontinuity affects the optimality of the obtained controller. However, pixel-based discontinuity could be ameliorated by increasing the number of pixels (minimizing the distance between adjacent pixels).

**Remark 5 (The Convexity of Unsafe Sets).** Note that only when the shape of the unsafe set is convex does the linearized safe boundary (20) entirely separate the unsafe region from the system. If the unsafe set is nonconvex, (20) might allow parts of the unsafe region to be on the same side as the system, potentially letting it enter these areas and causing danger. However, this problem could be ameliorated by shortening the system's step size, i.e., shortening the discretization time for updating new states in the discrete-time dynamic system (2).

#### D. CFTOC Problem

In Secs. IV-B and IV-C, we have demonstrated the linearization of system dynamics and the safety constraints using DHOCBF. This enables us to incorporate them as constraints in a convex MPC formulation at each iteration, which we refer to as Convex Finite-Time Constrained Optimization Control (CFTOC). This is solved at iteration  $j$  with optimization variables  $\mathbf{U}_t^j = [\mathbf{u}_{t,0}^j, \dots, \mathbf{u}_{t,N-1}^j]$  and  $\Omega_{t,i}^j = [\omega_{t,0,i}^j, \dots, \omega_{t,N,i}^j]$ , where  $i \in \{1, \dots, m_{\text{cbf}}\}$ .

---

#### CFTOC of iMPC-DHOCBF at iteration $j$ :

$$\min_{\mathbf{u}_{t,1}^j, \dots, \mathbf{u}_{t,m_{\text{cbf}}}^j} p(\mathbf{x}_{t,N}^j) + \sum_{k=0}^{N-1} q(\mathbf{x}_{t,k}^j, \mathbf{u}_{t,k}^j, \omega_{t,k,i}^j) \quad (22a)$$

$$\text{s.t. } \mathbf{x}_{t,k+1}^j - \bar{\mathbf{x}}_{t,k+1}^j = A^j(\mathbf{x}_{t,k}^j - \bar{\mathbf{x}}_{t,k}^j) + B^j(\mathbf{u}_{t,k}^j - \bar{\mathbf{u}}_{t,k}^j), \quad (22b)$$

$$\mathbf{u}_{t,k}^j \in \mathcal{U}, \mathbf{x}_{t,k}^j \in \mathcal{X}, \omega_{t,k,i}^j \in \mathbb{R}, \quad (22c)$$

$$\begin{aligned} \tilde{\psi}_{i-1}(\mathbf{x}_{t,k}^j) + \sum_{\nu=1}^i Z_{\nu,i}(1 - \gamma_i)^k \tilde{\psi}_0(\mathbf{x}_{t,\nu}^j) \geq \\ \omega_{t,k,i}^j Z_{0,i}(1 - \gamma_i)^k \tilde{\psi}_0(\mathbf{x}_{t,0}^j). \end{aligned} \quad (22d)$$


---

In the CFTOC, the linearized dynamics constraints in (12) and the linearized DHOCBF constraints in (18) are enforced with constraints (22b) and (22d) at each open-loop time step  $k \in \{0, \dots, N-1\}$ . The state and input constraints are considered in (22c). The slack variables are unconstrained because the primary objective of the optimization is to minimize the deviation from the nominal DHOCBF constraints with cost term  $q(\cdot, \cdot, \omega_{t,k,i}^j)$ , while ensuring feasibility of the optimization, as discussed in [31]. Note that, for ensuring the safety guarantee established by the DHOCBF, the constraints (22d) are enforced with  $i \in \{0, \dots, m_{\text{cbf}}\}$ , where  $Z_{\nu,i} \in \mathbb{R}$  is as defined in (18) with  $\nu \in \{0, \dots, i\}$ . The optimal decision variables of (22) at iteration  $j$  is a list of control input vectors as  $\mathbf{U}_t^{*,j} = [\mathbf{u}_{t,0}^{*,j}, \dots, \mathbf{u}_{t,N-1}^{*,j}]$  and a list of slack variable vectors as  $\Omega_{t,i}^{*,j} = [\omega_{t,0,i}^{*,j}, \dots, \omega_{t,N-1,i}^{*,j}]$ . For avoidance of unsafe sets, the CFTOC formulated in (22) only considers a single unsafe set. To accommodate  $p$  unsafe sets, the slack variable vectors  $\Omega_{t,i}^j$  (used in cost function and (22d)) need to be appropriately expanded to address  $p$  sets, and equation (22d) should also be expanded to address  $p$  sets. The CFTOC is solved iteratively in our proposed iMPC-DHOCBF and the solution can be extracted once the convergence criteria or the maximum iteration number  $j_{\text{max}}$  is reached, as shown in Fig. 1.

#### E. Complexity of iMPC-DHOCBF

1) *Size of Map and Network*: In Sec. IV-C.2, before we train the network, we need to gather as many sampled system's locations as possible across the map, while also identifying the nearest points on the boundaries of unsafe sets relative to the system. This means that the size of the map will influence the number of sampled locations and ground truth data. The larger the map, the greater the number of sampled locations and ground truth needed, which in turn

extends the time required to train the network. Additionally, the more complex the network structure (such as more hidden layers or more nodes), the longer it will take to train the network.

2) *Number of Unsafe Sets*: In (22), every system's state  $\mathbf{x}_{t,k}^j$  corresponds to a nearest point  $\tilde{\mathbf{x}}_{t,k}^j$  on each unsafe set, and each nearest point corresponds to a linearized DHOCBF (22d). Therefore, the more unsafe sets there are, the more DHOCBF constraints exist, leading to increased complexity in the CFTOC. One can choose to only consider unsafe sets within a certain range based on the current location to reduce complexity. This means that when the horizon  $N$  is large, the predictive capability of the MPC will be limited. Nonetheless, the complexity related to unsafe sets in our algorithm is lower than the state-of-the-art [40], because each polytopic unsafe set corresponds to multiple DHOCBFs.

3) *Horizon Length*: In (22), the horizon  $N$  results in a linear increase in the number of all constraints. Compared to distance constraints, DHOCBF constraints incorporate additional higher-order sufficient constraints to ensure safety. As discussed in [40], DHOCBF constraints enable effective avoidance behavior for unsafe sets with a smaller horizon length. One could consider to require the horizon of DHOCBF  $N_{\text{cbf}}$  smaller than  $N$  to reduce the complexity.

4) *Convergence Criterion*: In Fig. 1, the number of iterations at each time step is determined by the convergence criterion or  $j_{\text{max}}$ . One can flexibly choose which variables to include in the convergence criterion, e.g., state  $\mathbf{X}_t^{*,j}$ , input  $\mathbf{U}_t^{*,j}$ , or both state and input. Appropriately relaxing the convergence conditions (such as increasing the allowable error) or reducing  $j_{\text{max}}$  can both decrease the complexity of the algorithm.

5) *Highest Order of DHOCBF*: In (22), the highest order of DHOCBF  $m_{\text{cbf}}$  results in a linear increase in the number of DHOCBF constraints (22d). As discussed in Rem. 1, it is not necessary to formulate DCBF constraints up to the  $m^{\text{th}}$  order. In other words, the highest order for DHOCBF could be  $m_{\text{cbf}}$  with  $m_{\text{cbf}} \leq m$ . Making  $m_{\text{cbf}}$  smaller than  $m$  but larger than one will reduce the complexity of the algorithm without significantly compromising safety.

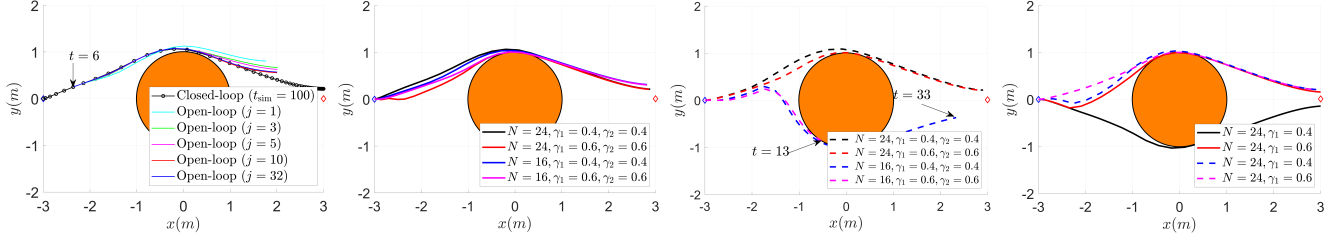
## V. CASE STUDY

In this section, we present numerical results to validate our proposed approach using a unicycle robot. First, we provide a performance comparison with the baseline NMPC-DHOCBF approach in Case Study I. In this comparison, we consider a circular obstacle as an unsafe set. The NMPC-DHOCBF is simply extended by using relaxed DHOCBF based on (11), as discussed in [32, Rem. 4]. In case studies II and III, we apply the proposed iMPC-DHOCBF to more complex maps. Animation videos can be found at <https://youtu.be/4t8TQ7gJUS8>.

#### A. Case Study I: Point Robot Avoidance of a Circular Obstacle with Known Boundary

Since the nearest point on a circle from a point outside the circle can be expressed by an accurate geometric equation,





(a) iMPC-DHOCBF when  $N = 24$ , (b) iMPC-DHOCBF with  $m_{\text{cbf}} = 2$ . (c) NMPC-DHOCBF with  $m_{\text{cbf}} = 2$ . (d) iMPC-DHOCBF and NMPC-DHOCBF with  $m_{\text{cbf}} = 1$ .

Fig. 4: Open-loop and closed-loop trajectories with controllers iMPC-DHOCBF (solid lines) and NMPC-DHOCBF (dashed lines): (a) several open-loop trajectories at different iterations predicted at  $t = 6$  and one closed-loop trajectory with controller iMPC-DHOCBF; (b) closed-loop trajectories with controller iMPC-DHOCBF with different choices of  $N$  and  $\gamma$ ; (c) closed-loop trajectories with controller NMPC-DHOCBF with different choices of  $N$  and  $\gamma$ . Note that two trajectories stop at  $t = 13$  and  $t = 33$  because of infeasibility; (d) closed-loop trajectories with controllers iMPC-DHOCBF and NMPC-DHOCBF with  $m_{\text{cbf}} = 1$ . Both methods work well for safety-critical navigation. This figure demonstrates that at a specific time step, iMPC-DHOCBF can iteratively drive the open-loop trajectory to converge to a local minimum while ensuring the safety of the closed-loop trajectory over  $t_{\text{sim}}$ .

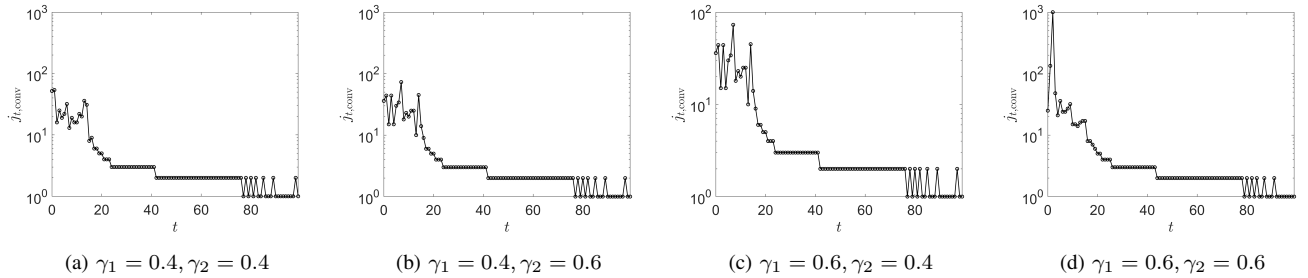


Fig. 5: Number of iterations  $j_{t,\text{conv}}$  at each time-step using controller iMPC-DHOCBF with different values of hyperparameters  $\gamma_1, \gamma_2$  with  $N = 24, m_{\text{cbf}} = 2$ . We can observe that, for almost all time-steps, the iterative optimization converges within 100 iterations ( $j_{t,\text{conv}} < 10^2$ ), which is affected very little with respect to hyperparameters.

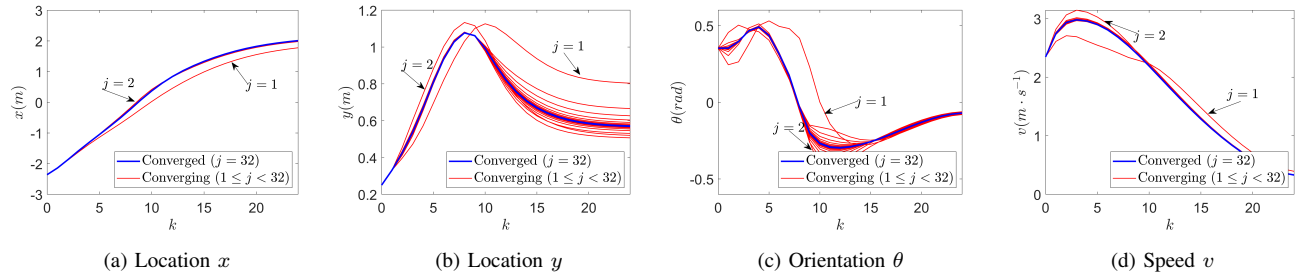


Fig. 6: Iterative convergence of all states at converged iteration  $j_{6,\text{conv}} = 32$  with  $N = 24, m_{\text{cbf}} = 2, \gamma_1 = \gamma_2 = 0.4$ . iMPC does help to optimize the cost function to reach local optimal minimum.

SBD is equivalent to finding tangent lines on this equation using derivatives, so we do not need to train a DNN in this subsection.

1) *System Dynamics*: Consider a discrete-time unicycle model in the form

$$\begin{bmatrix} x_{t+1} - x_t \\ y_{t+1} - y_t \\ \theta_{t+1} - \theta_t \\ v_{t+1} - v_t \end{bmatrix} = \begin{bmatrix} v_t \cos(\theta_t) \Delta t \\ v_t \sin(\theta_t) \Delta t \\ 0 \\ 0 \end{bmatrix} + \begin{bmatrix} 0 & 0 \\ 0 & 0 \\ \Delta t & 0 \\ 0 & \Delta t \end{bmatrix} \begin{bmatrix} u_{1,t} \\ u_{2,t} \end{bmatrix}, \quad (23)$$

where  $\mathbf{x}_t = [x_t, y_t, \theta_t, v_t]^T$  captures the 2-D location, heading angle, and linear speed;  $\mathbf{u}_t = [u_{1,t}, u_{2,t}]^T$  represents angular velocity ( $u_1$ ) and linear acceleration ( $u_2$ ), respectively. The system is discretized with  $\Delta t = 0.1$  and the total number

of discretization steps  $t_{\text{sim}}$  equals  $T$  in Problem. 1. System (23) is subject to the following state and input constraints:

$$\begin{aligned} \mathcal{X} &= \{\mathbf{x}_t \in \mathbb{R}^4 : -10 \cdot \mathcal{I}_{4 \times 1} \leq \mathbf{x}_t \leq 10 \cdot \mathcal{I}_{4 \times 1}\}, \\ \mathcal{U} &= \{\mathbf{u}_t \in \mathbb{R}^2 : [-7, -5]^T \leq \mathbf{u}_t \leq [7, 5]^T\}. \end{aligned} \quad (24)$$

2) *System Configuration*: The initial state is  $[-3, 0, 0, 0]^T$  and the target state is  $[3, 0.01, 0, 0]^T$ , which are marked as blue and red diamonds in Fig. 4. The circular obstacle is centered at  $(0, 0)$  with  $r = 1$ , which is displayed in orange. The other reference vectors are  $\mathbf{u}_r = [0, 0]^T$  and  $\omega_r = [1, 1]^T$ . We use the offset  $y = 0.01m$  in  $\mathbf{x}_r$  to prevent singularity of the optimization problem.

3) *DHOCBF*: As a candidate DHOCBF function  $\psi_0(\mathbf{x}_t)$ , we choose a quadratic distance function for circular obstacle

avoidance  $h(\mathbf{x}_t) = (x_t - x_0)^2 + (y_t - y_0)^2 - r^2$ , where  $(x_0, y_0)$  and  $r$  denote the obstacle center location and radius, respectively. The linearized DHOCBF  $\tilde{\psi}_0(\mathbf{x}_{t,k}^j)$  in (14) is defined as  $\tilde{\psi}_0(\mathbf{x}_{t,k}^j) := h_{\parallel}(\mathbf{x}_{t,k}^j, \tilde{\mathbf{x}}_{t,k}^j)$ , with

$$h_{\parallel}(\mathbf{x}_{t,k}^j, \tilde{\mathbf{x}}_{t,k}^j) = (\tilde{x}_{t,k}^j - x_0)x_{t,k}^j + (\tilde{y}_{t,k}^j - y_0)y_{t,k}^j - (r^2 - x_0^2 - y_0^2 + \tilde{x}_{t,k}^j x_0 + \tilde{y}_{t,k}^j y_0), \quad (25)$$

where  $h_{\parallel}(\mathbf{x}_{t,k}^j, \tilde{\mathbf{x}}_{t,k}^j)$  is the linearized boundary, whose relative degree is 2;  $(\tilde{x}_{t,k}^j, \tilde{y}_{t,k}^j)$  denotes the tangent point of the circular boundary  $h(\mathbf{x}_t)$ . From (19), we have  $Z_{0,2} = \gamma_1 - 1$ ,  $Z_{1,2} = -1$ ,  $Z_{0,1} = 1$ ,  $Z_{2,2} = Z_{1,1} = 0$ .

4) *MPC Design*: The cost function of the CFTOC problem (22) consists of stage cost  $q(\mathbf{x}_{t,k}^j, \mathbf{u}_{t,k}^j, \omega_{t,k,i}^j) = \sum_{k=0}^{N-1} (\|\mathbf{x}_{t,k}^j - \mathbf{x}_r\|_Q^2 + \|\mathbf{u}_{t,k}^j - \mathbf{u}_r\|_R^2 + \|\omega_{t,k,i}^j - \omega_r\|_S^2)$  and terminal cost  $p(\mathbf{x}_{t,N}^j) = \|\mathbf{x}_{t,N}^j - \mathbf{x}_r\|_P^2$ , where  $Q = P = 10 \cdot \mathcal{I}_4$ ,  $R = \mathcal{I}_2$  and  $S = 1000 \cdot \mathcal{I}_2$ .

5) *Convergence Criteria*: We use the following absolute and relative convergence functions as convergence criteria mentioned in Fig. 1:

$$e_{\text{abs}}(\mathbf{X}_t^{*,j}, \mathbf{U}_t^{*,j}) = \|\mathbf{X}_t^{*,j} - \bar{\mathbf{X}}_t^{*,j}\| \\ e_{\text{rel}}(\mathbf{X}_t^{*,j}, \mathbf{U}_t^{*,j}, \bar{\mathbf{X}}_t^j, \bar{\mathbf{U}}_t^j) = \|\mathbf{X}_t^{*,j} - \bar{\mathbf{X}}_t^{*,j}\| / \|\bar{\mathbf{X}}_t^{*,j}\|. \quad (26)$$

The iterative optimization stops when  $e_{\text{abs}} < \varepsilon_{\text{abs}}$  or  $e_{\text{rel}} < \varepsilon_{\text{rel}}$ , where  $\varepsilon_{\text{abs}} = 10^{-4}$ ,  $\varepsilon_{\text{rel}} = 10^{-2}$  and the maximum iteration number is set as  $j_{\text{max}} = 1000$ . To ensure a fair comparison with NMPC-DHOCBF, the hyperparameters  $P, Q, R, S$  are kept consistent across all configurations.

6) *Solver Configurations and CPU Specs*: For iMPC-DHOCBF, we used OSQP [42] to solve the convex optimizations at all iterations. The baseline approach NMPC-DHOCBF is open-source, and was solved using IPOPT [43] with the modeling language Yalmip [44]. We used a Windows desktop with Intel Core i7-8700 (CPU 3.2 GHz) running Matlab for all computations.

7) *Iterative Convergence*: The iterative convergence is shown in Figs. 4a, 5 and 6. Fig. 4a shows the closed-loop trajectory (the black line) generated by solving the iMPC-DHOCBF until the converged iteration  $j_{t,\text{conv}}$  from  $t = 0$  to  $t = t_{\text{sim}} = 100$  and open-loop iteratively converging trajectories (colored lines) at different iterations at  $t = 6$ . Fig. 6 presents more details on the iterative convergence of states at different iterations at  $t = 6$  with number of iterations  $j_{t,\text{conv}} = 32$ . We note that, after around 10 iterations, the converging lines for the states (red lines) nearly overlap with the converged line (blue line) in Fig. 6. This verifies the relations of the converging trajectory (red line) and the converged trajectory (blue line) in Fig. 4a. The optimization is shown to converge at iteration  $j_{t,\text{conv}}$  at time step  $t$  for different hyperparameters  $\gamma$  under specific convergence criteria (26), shown in Fig. 5. We can see that for the first 15 time steps the iMPC-DHOCBF triggers more iterations to drive the system to avoid the obstacle than time steps after 20 where the system already passes the obstacle. The maximum converged iteration  $j_{t,\text{conv}}$  is 1000 at time step  $t = 2$  in Fig. 5d with  $\gamma_1 = \gamma_2 = 0.6$ , which reveals that the peak of the

converged iteration over time increases if we choose larger  $\gamma$ . For the majority of the time-steps, the iterative optimization converges within 100 iterations ( $j_{t,\text{conv}} < 100$ ).

8) *Convergence with Different Hyperparameters*: Fig. 4b, 4c and 4d show the closed-loop trajectories generated by solving iMPC-DHOCBF (solid lines) and NMPC-DHOCBF (dashed lines) at converged iteration  $j_{t,\text{conv}}$  from  $t = 0$  to  $t = t_{\text{sim}} = 45$  with different hyperparameters. Both controllers show good performance on obstacle avoidance. Based on black, red, blue and magenta lines with the highest order of CBF constraint  $m_{\text{cbf}} = 2$  in Fig. 4b and 4c, as  $\gamma_1, \gamma_2$  become smaller, the system tends to turn further away from the obstacle when it is getting closer to obstacle, which indicates a safer control strategy. From the lines in Fig. 4d where  $m_{\text{cbf}} = 1$ , we can see that the system can still safely navigate around the obstacle, although it turns away from the obstacle later than when having one more CBF constraint in Fig. 4b and 4c, indicating that having CBF constraints up to the relative degree enhances safety. The blue and magenta dashed lines in Fig. 4c stop at  $t = 33$  and  $t = 13$  with  $N = 16$  as infeasibility happens, which shows that a large horizon is needed to generate complete closed-loop trajectories for some hyperparameters by NMPC-DHOCBF, while iMPC-DHOCBF shows less reliance on selection of horizon since it can generate complete closed-loop trajectories with both  $N = 16$  and  $N = 24$ , as shown in Fig. 4b.

9) *Computation Time*: In order to compare computational times between our proposed iMPC-DHOCBF and the baseline NMPC-DHOCBF, 1000 independent randomized safe states are generated in state constraint  $\mathcal{X}$  in (24). To make a fair comparison, both approaches use the same  $N$  and  $m_{\text{cbf}}$  and the computational time and feasibility are evaluated at those randomized sample states. The distributions of the computation times and infeasibility rates in Tab. II and Tab. III correspond to generating one time-step trajectories. The mean and standard deviation of computation times increase if the horizon  $N$  or  $m_{\text{cbf}}$  become larger for NMPC-DHOCBF in Tab. II and Tab. III. Different from NMPC-DHOCBF, the computing time is not heavily influenced by  $N$  and  $m_{\text{cbf}}$  for iMPC-DHOCBF. Based on the data from the two tables, we also notice that larger hyperparameter values for  $\gamma$  will slightly reduce the computation speed for both methods, which is discussed in Sec. V-A.7 and can be attributed to the rise of converged iteration  $j_{t,\text{conv}}$ . Compared to NMPC-DHOCBF, the computing speed of our proposed method is much faster with the improvement in computation time directly proportional to the horizon, *e.g.*,  $100 \sim 300$  times faster than the baseline given the chosen hyperparameters.

10) *Optimization Feasibility*: The rate of infeasibility increases if the horizon  $N$  increases or  $m_{\text{cbf}}$  is lower for iMPC-DHOCBF. However, these two hyperparameters are shown not to affect the infeasibility rate of the NMPC-DHOCBF method proportionally. As the horizon increases, the infeasibility rate of iMPC-DHOCBF outperforms that of NMPC-DHOCBF. The main reasons for this come from the difference in the convergence criteria, warm start and relaxation techniques for CBF constraints, discussed

Approaches		$N = 4$	$N = 8$	$N = 12$	$N = 16$	$N = 20$	$N = 24$
NMPC-DHOCBF ( $m_{\text{cbf}} = 2$ )	mean / std (s)	$3.687 \pm 6.360$	$23.882 \pm 17.988$	$27.329 \pm 20.115$	$28.953 \pm 22.058$	$30.970 \pm 23.564$	$29.929 \pm 22.105$
	infeas. rate	5.8%	27.5%	21.1%	16.4%	14.5%	14.4%
NMPC-DHOCBF ( $m_{\text{cbf}} = 1$ )	mean / std (s)	$2.933 \pm 4.678$	$19.077 \pm 14.024$	$20.418 \pm 15.401$	$22.749 \pm 17.039$	$24.053 \pm 17.811$	$25.365 \pm 18.211$
	infeas. rate	6.3%	13.9%	13.0%	14.6%	13.8%	15.4%
iMPC-DHOCBF ( $m_{\text{cbf}} = 2$ )	mean / std (s)	$0.135 \pm 0.294$	$0.104 \pm 0.242$	$0.102 \pm 0.217$	$0.131 \pm 0.301$	$0.165 \pm 0.400$	$0.135 \pm 0.274$
	infeas. rate	6.3%	8.0%	10.4%	10.9%	10.9%	10.2%
iMPC-DHOCBF ( $m_{\text{cbf}} = 1$ )	mean / std (s)	$0.131 \pm 0.286$	$0.114 \pm 0.260$	$0.109 \pm 0.237$	$0.137 \pm 0.316$	$0.173 \pm 0.414$	$0.152 \pm 0.317$
	infeas. rate	6.3%	8.0%	10.4%	10.9%	10.9%	11.1%

TABLE II: Statistical benchmark for computation time and feasibility between NMPC-DHOCBF and iMPC-DHOCBF with randomized states. The target position is shared among four approaches and the hyperparameters are fixed as  $\gamma_1 = \gamma_2 = 0.4$  for all random scenarios.

Approaches		$N = 4$	$N = 8$	$N = 12$	$N = 16$	$N = 20$	$N = 24$
NMPC-DHOCBF ( $m_{\text{cbf}} = 2$ )	mean / std (s)	$3.744 \pm 6.445$	$28.779 \pm 20.755$	$31.319 \pm 21.921$	$33.678 \pm 25.328$	$36.430 \pm 26.959$	$39.543 \pm 29.941$
	infeas. rate	5.6%	28.0%	20.9%	16.8%	17.0%	14.6%
NMPC-DHOCBF ( $m_{\text{cbf}} = 1$ )	mean / std (s)	$3.032 \pm 4.536$	$21.414 \pm 16.518$	$23.121 \pm 17.544$	$24.011 \pm 17.711$	$26.599 \pm 19.480$	$29.671 \pm 20.026$
	infeas. rate	6.4%	17.0%	15.2%	15.5%	16.7%	13.2%
iMPC-DHOCBF ( $m_{\text{cbf}} = 2$ )	mean / std (s)	$0.158 \pm 0.326$	$0.134 \pm 0.279$	$0.163 \pm 0.353$	$0.163 \pm 0.373$	$0.184 \pm 0.398$	$0.164 \pm 0.344$
	infeas. rate	6.1%	8.0%	10.2%	10.7%	10.8%	10.8%
iMPC-DHOCBF ( $m_{\text{cbf}} = 1$ )	mean / std (s)	$0.167 \pm 0.340$	$0.139 \pm 0.291$	$0.170 \pm 0.362$	$0.170 \pm 0.379$	$0.201 \pm 0.435$	$0.176 \pm 0.378$
	infeas. rate	6.1%	8.0%	10.2%	10.7%	10.8%	10.8%

TABLE III: Statistical benchmark between NMPC-DHOCBF and iMPC-DHOCBF with the same randomized states as in Tab. II. The target position is shared among four approaches and the hyperparameters are fixed as  $\gamma_1 = \gamma_2 = 0.6$  for all scenarios. Based on Tab. II and Tab. III we conclude that iMPC-DHOCBF outperforms NMPC-DHOCBF in computing time and infeasibility rate.

in ReMs. 2 and 3. The NMPC-DHOCBF under IPOPT should have more strict convergence criteria compared to iMPC-DHOCBF, which obviously limits its feasibility if the number of horizon is large. Besides, the NMPC-DHOCBF should have a more effectively refined warm start compared to the iMPC-DHOCBF. Furthermore, NMPC-DHOCBF is equipped with relaxed nonlinear CBF constraints (15), while iMPC-DHOCBF has relaxed linear CBF constraints (18). The linearization of the CBF constraints reduces the feasibility region in the state space, as illustrated in Fig. 2. These meet the expectation of slight decreased feasibility rate of iMPC-DHOCBF when horizon length is small. However, we can see that the decline in feasibility rate due to relaxed technique and warm start is noticeably outperformed by flexible convergence criteria with larger horizon length  $N$  in Tab. II and III, which validates our linearization technique in the iterative optimization.

### B. Case Study II: Point Robot Avoidance of Irregular Obstacles with Unknown Boundaries

In the maps in this subsection, there are both convex and nonconvex obstacles, and the nearest points on their boundaries to the robot are difficult to represent with continuous and accurate equations. Therefore, we will train a DNN for the SBD to predict the nearest points.

1) *System Dynamics*: We consider the same dynamics as in Sec. V-A with  $\Delta t = 0.05$ . System (23) is subject to the following state and input constraints:

$$\begin{aligned} \mathcal{X} &= \{\mathbf{x}_t \in \mathbb{R}^4 : -10 \cdot \mathcal{I}_{4 \times 1} \leq \mathbf{x}_t \leq 10 \cdot \mathcal{I}_{4 \times 1}\}, \\ \mathcal{U} &= \{\mathbf{u}_t \in \mathbb{R}^2 : -10 \cdot \mathcal{I}_{2 \times 1} \leq \mathbf{u}_t \leq 10 \cdot \mathcal{I}_{2 \times 1}\}. \end{aligned} \quad (27)$$

2) *System Configuration*: The five different start points are  $(-2, -2)$ ,  $(-2, 2)$ ,  $(-0.8, -0.8)$ ,  $(0, 0.8)$ ,  $(1.2, 0.4)$  and the corresponding end points are  $(2, 2)$ ,  $(2, -2)$ ,  $(0, 0.8)$ ,  $(1.2, 0.4)$ ,  $(0, 0)$ , which are marked as solid dots in Fig. 9.

The robot can stop when it reaches inside the target areas centered at end points with a radius of 0.1. The initial and reference linear speeds are 0 and the initial and reference heading angles are calculated by  $\theta_0 = \theta_r = \text{atan2}(\frac{y_r - y_t}{x_r - x_t})$ , where  $(x_t, y_t)$  denotes the current location and  $(x_r, y_r)$  denotes the end point. Five obstacles are displayed in red, with convex and nonconvex shapes. The other reference vectors are  $\mathbf{u}_r = [0, 0]^T$  and  $\omega_r = \mathcal{I}_{1 \times 10}$ .

3) *Map Processing*: The scope of the map is  $x \in [-2.5, 2.5]$  and  $y \in [-2, 2]$ . The coordinates of pixels on the boundaries of obstacles are manually chosen, and we limit the number of boundary pixels for each obstacle to 100.

4) *SBD Training and Evaluation*: Our neural network has 9 hidden layers and begins with 512 nodes in the first hidden layer, denoted as  $h_0$ . The subsequent layers' dimensions are defined by (21). Within the range of the map, we extracted 154993 data entries (random locations across the entire map) for training and another 25741 (random locations outside of obstacles) for testing. For  $p$  obstacles, we use the following Mean Squared Error (MSE) equation to evaluate the accuracy of the SBD's predictions of the nearest points on obstacle boundaries relative to the robot:

$$\text{MSE} = \frac{1}{p} \sum_{i=1}^p [(x_i - \tilde{x}_i)^2 + (y_i - \tilde{y}_i)^2], \quad (28)$$

where  $(x_i, y_i)$  denotes the coordinate of the ground truth of nearest point and  $(\tilde{x}_i, \tilde{y}_i)$  denoted the coordinate of predicted nearest point from SBD.

5) *DHOCBF*: Since the predicted nearest points  $\tilde{\mathbf{x}}_{t,k}^j$  can be obtained from the output of the SBD, we choose (20) as a linearized DHOCBF whose relative degree is 2. Note that five obstacles correspond to five linearized DHOCBFs. The sequence of linearized DHOCBF is defined by (14). From (19), we have  $Z_{0,2} = \gamma_1 - 1$ ,  $Z_{1,2} = -1$ ,  $Z_{0,1} = 1$ ,  $Z_{2,2} = Z_{1,1} = 0$ .

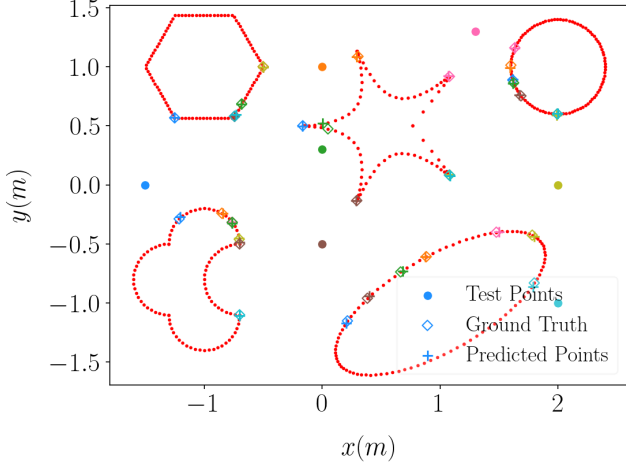


Fig. 7: Demonstration of SBD Prediction Performance. Seven solid dots represent the positions of seven different robots. Diamonds indicate the ground truth of the nearest points on the corresponding obstacles, while the plus symbols represent the positions of the nearest points predicted by the SBD based on the robots’ locations. Most of the predicted nearest points are very close to the ground truth, with only the prediction corresponding to the green dot showing a relatively large discrepancy from the ground truth.

6) *MPC Design*: The cost function of the CFTOC problem (22) consists of stage cost  $q(\mathbf{x}_{t,k}^j, \mathbf{u}_{t,k}^j, \omega_{t,k,i}^j) = \sum_{k=0}^{N-1} (\|\mathbf{x}_{t,k}^j - \mathbf{x}_r\|_Q^2 + \|\mathbf{u}_{t,k}^j - \mathbf{u}_r\|_R^2 + \|\omega_{t,k,i}^j - \omega_r\|_S^2)$  and terminal cost  $p(\mathbf{x}_{t,N}^j) = \|\mathbf{x}_{t,N}^j - \mathbf{x}_r\|_P^2$ , where  $Q = P = 10 \cdot \mathcal{I}_4$ ,  $R = \mathcal{I}_2$  and  $S = 1000 \cdot \mathcal{I}_{10}$ .

7) *Convergence Criteria*: We use the same absolute and relative convergence functions from (26) as convergence criteria mentioned in Fig. 1. The iterative optimization stops when  $e_{\text{abs}} < \varepsilon_{\text{abs}}$  or  $e_{\text{rel}} < \varepsilon_{\text{rel}}$ , where  $\varepsilon_{\text{abs}} = 10^{-2}$ ,  $\varepsilon_{\text{rel}} = 10^{-2}$ . In Fig. 5 we observed that the peak of the converged iteration over time increases if we choose larger  $\gamma$ , therefore, the hyperparameter related to the decay rate is set to a relatively smaller value as  $\gamma_1 = 0.1$  to reduce the needed maximum iteration number which is set as  $j_{\text{max}} = 30$ .

8) *Solver Configurations and CPU Specs*: For iMPC-DHOCBF, we used OSQP [42] in Python to solve the convex optimizations at all iterations. For model training and inference, we utilize Pytorch as our primary framework. The training was conducted on a Linux desktop equipped with a Nvidia RTX 4090 graphics card to leverage GPU capabilities. For inference, we use a Linux laptop with AMD Ryzen 7 5800U with all inferencing performed only on the CPU.

9) *SBD Prediction Accuracy*: The prediction accuracy of SBD is demonstrated in Figs. 7 and 8. In Fig. 7, we selected seven different locations from testing data on the map, each represented by a solid dot in a corresponding color. For these seven locations, there are five reference nearest points on the obstacle boundaries (diamonds) and the nearest points predicted by the SBD (plus symbols). When the robot is near the convex boundary of an obstacle, the predicted nearest points closely match the references. However, near

concave boundaries, there is some deviation, though not substantial. Figure 8 shows the relationship between the SBD’s prediction error (MSE) and the robot’s positions in a 3D chart. Since testing data are from outside the obstacles, MSE within obstacles is not shown (darkest areas). The MSE is relatively small near convex boundaries (darker colors) and larger near concave boundaries (brighter colors). Higher MSE values are observed near concave boundaries and extend along certain radial lines due to the presence of multiple equidistant nearest points on the obstacle boundaries relative to these lines. During data collection, one of the equidistant points is randomly chosen as a reference. This randomness causes the trained SBD to predict a nearest point based on a blend of these equidistant points, resulting in significant discrepancies from the chosen reference point and a large MSE. Moreover, we noted that the largest MSE occurs along the line at  $y = 0.5$ . This is because when extracting pixels from the boundary of the pentagram-shaped obstacle, we limited the number of pixels to 100 to reduce the complexity as discussed in Sec. IV-C.2 under **Map Processing**, resulting in sparse pixel distribution near  $y = 0.5$  (also see Figure 7). This sparsity contributes to the higher MSE along this line. Increasing the number of pixels on the obstacle boundary can help reduce SBD prediction error.

10) *Safe Trajectory Generation*: Five safe closed-loop trajectories start from corresponding start points and end in corresponding target areas, shown in Fig. 9. We observe that even with multiple obstacles, including those with complex shapes like the sharp protrusions of a pentagram, the robot navigates safely in free space, regardless of proximity to obstacles or path length. However, the trajectory appears zigzagged and unsmooth in some areas. This is because the robot’s trajectory is not generated by tracking a safe smooth path but is directly guided by the endpoint, with no global map or obstacle information. It moves locally, adjusting back and forth to find a feasible trajectory. Additionally, the absence of adaptive warm start and convergence criteria contributes to the unsmooth trajectory.

11) *Computation Time and Feasibility*: In order to compare computational time and feasibility of our proposed iMPC-DHOCBF under different hyperparameters, 1000 independent randomized safe states are generated in state constraint  $\mathcal{X}$  in (27). To make a fair comparison, the randomized states and end points are shared among four sets of hyperparameters and the other irrelevant hyperparameters are fixed for all scenarios. We can observe in Tab. IV that as  $N$  increases, the computation time per step significantly increases. Similarly, when  $m_{\text{cbf}}$  increases or  $\gamma_1, \gamma_2$  increase, the computation time per step also rises. The computation time is primarily affected by  $N$  and  $m_{\text{cbf}}$  because each call to the SBD consumes a certain amount of time. Increases in  $N$  and  $m_{\text{cbf}}$  linearly raise the number of SBD calls, thus significantly increasing the computation time per step. However, these hyperparameters are shown not to affect the infeasibility rate of the iMPC-DHOCBF method proportionally. Compared to the iMPC-DHOCBF in Tab. II and Tab. III, iMPC-DHOCBF triggering SBD still maintains a fast

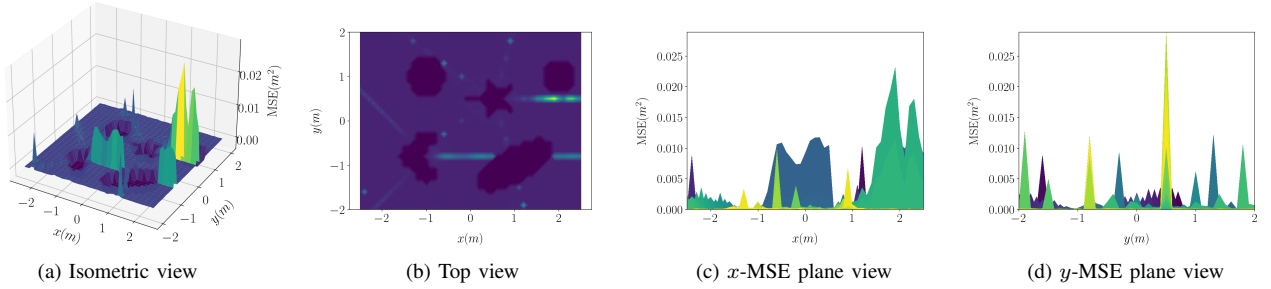


Fig. 8: 3D visualization of the MSE of the testing data.  $x$  and  $y$  represent the positions of the testing points, while MSE represents the prediction error corresponding to the point  $(x, y)$ . The maximum MSE is 0.029 at  $(1.9, 0.5)$ .

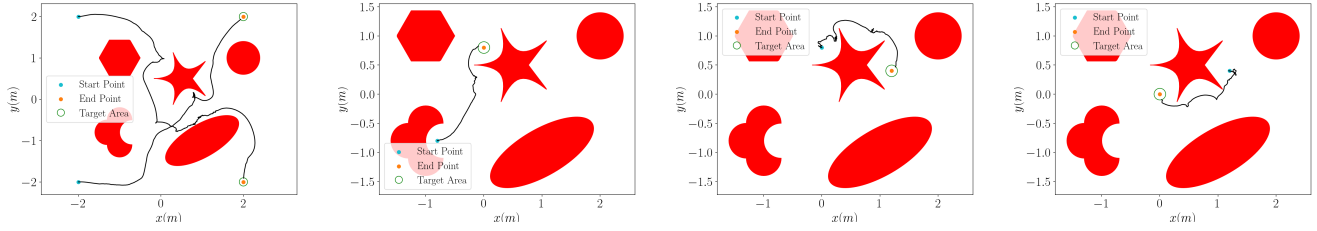


Fig. 9: Five closed-loop trajectories (black) with different start and end points controlled by iMPC-DHOCBF with  $m_{cbf} = 1$ ,  $N = 24$ ,  $\gamma_1 = 0.1$ . The obstacles are shown in red. Note that unlike [40], in which the authors use motion planning to find a safe desired path for the robot to follow, we do not create a safe desired path to guide the robot. As a result, the generated trajectory is **nonsmooth**. This setup is intended to increase the difficulty of obstacle avoidance for the robot. The animation video can be found at <https://youtu.be/4t8TQ7gJUS8>.

Approaches		$N = 4$	$N = 8$	$N = 12$	$N = 16$	$N = 20$	$N = 24$
iMPC-DHOCBF ( $m_{cbf} = 2, \gamma_1 = \gamma_2 = 0.1$ )	mean / std (s)	$0.029 \pm 0.020$	$0.065 \pm 0.042$	$0.126 \pm 0.069$	$0.202 \pm 0.090$	$0.340 \pm 0.126$	$0.446 \pm 0.138$
	infeas. rate	4.5%	5.4%	5.0%	6.0%	5.9%	6.4%
iMPC-DHOCBF ( $m_{cbf} = 1, \gamma_1 = 0.1$ )	mean / std (s)	$0.028 \pm 0.020$	$0.053 \pm 0.030$	$0.108 \pm 0.055$	$0.167 \pm 0.068$	$0.235 \pm 0.082$	$0.374 \pm 0.106$
	infeas. rate	4.9%	5.4%	4.9%	5.4%	5.0%	5.3%
iMPC-DHOCBF ( $m_{cbf} = 2, \gamma_1 = \gamma_2 = 0.2$ )	mean / std (s)	$0.031 \pm 0.020$	$0.073 \pm 0.046$	$0.141 \pm 0.070$	$0.242 \pm 0.091$	$0.416 \pm 0.113$	$0.545 \pm 0.144$
	infeas. rate	4.6%	4.9%	6.3%	7.5%	9.3%	10.9%
iMPC-DHOCBF ( $m_{cbf} = 1, \gamma_1 = 0.2$ )	mean / std (s)	$0.032 \pm 0.024$	$0.071 \pm 0.040$	$0.139 \pm 0.055$	$0.217 \pm 0.063$	$0.296 \pm 0.063$	$0.435 \pm 0.063$
	infeas. rate	4.5%	4.6%	4.3%	4.9%	4.5%	5.0%

TABLE IV: Statistical benchmark for computation time and feasibility for iMPC-DHOCBF with SBD. The randomized states and end points are shared among four approaches and the other irrelevant hyperparameters are fixed for all scenarios.

computation speed per step and has a lower infeasibility rate, even in a more complex map.

### C. Case Study III: Circular Robot Navigation in A Narrow Track with Unknown Boundaries

Similar to Sec. V-B, we will train a DNN for the SBD to predict the nearest points.

1) *System Dynamics*: The robot is circular with a radius of 0.4, and its geometric center possesses the same dynamics as in Sec. V-A with  $\Delta t = 0.05$ . System (23) is subject to the same state and input constraints shown in (27).

2) *System Configuration*: We plan to generate five connected closed-loop trajectories, where the start point of each subsequent trajectory is the end point of the previous one. The initial location and four waypoints marked as solid dots are  $(4, -4.5)$ ,  $(2.5, -2)$ ,  $(2, 2)$ ,  $(-4, 2)$ ,  $(-7.5, -3.3)$  and the end point is  $(-2.5, -4.25)$  in Fig. 11. The robot can terminate the current trajectory when its center reaches inside circles centered at each waypoint with a radius of 0.1 and then begin a second trajectory. The initial and reference

linear speeds are 0 and the initial and reference heading angles are calculated by  $\theta_0 = \theta_r = \text{atan2}(\frac{y_r - y_t}{x_r - x_t})$ , where  $(x_t, y_t)$  denotes the current location and  $(x_r, y_r)$  denotes each waypoint. The robot's operating area is a narrow track enclosed by two bar-shaped obstacles with point contact connections. The width of the track varies within  $[\sqrt{2}, 2]$ , and the track shape consists of Z-shaped bends and S-shaped bends. The other reference vectors are  $\mathbf{u}_r = [0, 0]^T$  and  $\omega_r = \mathcal{I}_{1 \times 4}$ .

3) *Map Processing*: The scope of the map is  $x \in [-10, 6]$  and  $y \in [-6, 6]$ . We manually set the coordinates of pixels on the two obstacle boundaries in contact with the track, limiting each boundary to a maximum of 400 pixels. This is equivalent to enclosing the free track space with a closed shape formed by two boundary lines from the two obstacles.

4) *SBD Training and Evaluation*: Our neural network's structure is completely identical to that in V-B.4. Within the range of the map, we extracted 714875 data entries (random locations across the entire map) for training and another 48761 (random locations inside the track) for testing. We

use the same MSE equation (28) to evaluate the accuracy of the SBD’s predictions of the nearest points on obstacle boundaries relative to the robot.

5) *DHOCBF*: The design of DHOCBFs is exactly the same as that in V-B.5. Note that our robot is circular, therefore, Eqn. (20), which imposes constraints on the robot’s center position, should be shifted a distance equal to the radius toward the robot’s center.

6) *MPC Design*: The cost function of the CFTOC problem (22) consists of stage cost  $q(\mathbf{x}_{t,k}^j, \mathbf{u}_{t,k}^j, \omega_{t,k,i}^j) = \sum_{k=0}^{N-1} (\|\mathbf{x}_{t,k}^j - \mathbf{x}_r\|_Q^2 + \|\mathbf{u}_{t,k}^j - \mathbf{u}_r\|_R^2 + \|\omega_{t,k,i}^j - \omega_r\|_S^2)$  and terminal cost  $p(\mathbf{x}_{t,N}^j) = \|\mathbf{x}_{t,N}^j - \mathbf{x}_r\|_P^2$ , where  $Q = P = 10 \cdot \mathcal{I}_4$ ,  $R = \mathcal{I}_2$  and  $S = 1000 \cdot \mathcal{I}_4$ .

7) *Convergence Criteria*: The design of convergence criteria is exactly the same as that in V-B.7.

8) *Solver Configurations and CPU Specs*: The design of solver configurations and CPU specifications is exactly the same as that in V-B.8.

9) *SBD Prediction Accuracy*: The prediction accuracy of SBD is demonstrated in Fig. 10. In Fig. 10, we have illustrated the relationship between the SBD’s prediction error (MSE) and the robot’s various positions using a 3D chart from multiple perspectives. Since the testing data was selected from the robot track, the MSE outside the track on the chart is devoid of values and the darkest. We can observe that when the robot’s position is near the convex boundary of the track, the MSE of the predicted nearest point is relatively small (indicated by darker colors). Conversely, when the robot’s position is near the concave boundary of the track, the MSE of the predicted nearest point is relatively large (indicated by brighter colors), which is similar to the observations made in Fig. 8. Unlike Fig. 8, not all concave boundary areas exhibit large prediction errors, e.g., the concave boundary sections of Z-shaped bends display a linear pattern of increasing MSE while concave boundary sections of the S-shaped bends do not show large MSE. This shows that the concavity of a boundary relative to a point outside the boundary also affects the MSE of nearest point prediction. The greater the concavity, the larger the prediction error. Additionally, we noted that the largest MSE is 0.690, which is much larger than the maximum MSE in Fig. 8. The peak MSEs in Fig. 10 are also significantly larger than that in Fig. 8. This is because the size of the map also affects the prediction error. Large maps often require significantly large quantities of training data to reduce prediction errors to very low levels. During the process of hyperparameter tuning, in locations where the MSE is relatively large, we can appropriately reduce the weight  $S$  of the slack variable to ensure that the optimization remains feasible and that the safety constraints are not violated.

10) *Safe Trajectory Generation*: Five closed-loop trajectories connecting each waypoint are shown in Fig. 11. We can see that even within a narrow track, sometimes requiring sharp turns, the robot can still navigate safely in free space. Note that even the robot is directly guided by each waypoint, compared to Fig. 9, the robot’s trajectory in Fig. 11 is smoother. This is because under the constraints of a narrow

track, the robot’s path to the end point is more defined, resulting in less wandering. In Fig. 12, we can observe the trends in the robot’s states and inputs as they change with each time step during its movement. Since the reference values for  $v, u_1, u_2$  in the cost function are all zero, they fluctuate within a small range around zero as a baseline. All system variables are subject to the constraints (27), which highlights the safety and planning features under constraints of our implementation.

## VI. CONCLUSION & FUTURE WORK

We proposed an iterative convex optimization procedure for safety-critical model predictive control design. Central to our approach is a learning-based safety boundary detector (SBD) to predict linearized safety boundaries for unsafe sets with arbitrary shapes, the transformation of these safety boundaries into discrete-time high-order control barrier functions (DHOCBFs), and relaxations for the system dynamics and for DHOCBF in the form of linearized constraints. We validated the proposed iMPC-DHOCBF approach by applying it to a unicycle robot navigating through three different environments, each containing respectively circular obstacles, irregular obstacles, and a narrow track. We noticed that the computation times for the iMPC-DHOCBF method significantly outperform the ones corresponding to the baseline, usually with even higher feasibility rate. Moreover, the unicycle can safely navigate through complex environments without following a pre-designed path. There are still some limitations of iMPC-DHOCBF with SBD that could be ameliorated. One limitation of the proposed method is for locations near the concave boundary of an unsafe set, the SBD’s prediction error for the nearest point remains relatively large. Another limitation is that the feasibility of the optimization and system safety are not always guaranteed at the same time in the whole state space. We will address these limitations in future work.

## REFERENCES

- [1] A. D. Ames, J. W. Grizzle, and P. Tabuada, “Control barrier function based quadratic programs with application to adaptive cruise control,” in *53rd IEEE Conference on Decision and Control*, 2014, pp. 6271–6278.
- [2] A. D. Ames, X. Xu, J. W. Grizzle, and P. Tabuada, “Control barrier function based quadratic programs for safety critical systems,” *IEEE Transactions on Automatic Control*, vol. 62, no. 8, pp. 3861–3876, 2016.
- [3] J. Zeng, B. Zhang, and K. Sreenath, “Safety-critical model predictive control with discrete-time control barrier function,” in *2021 American Control Conference (ACC)*, 2021, pp. 3882–3889.
- [4] M. Diehl, H. G. Bock, and J. P. Schlöder, “A real-time iteration scheme for nonlinear optimization in optimal feedback control,” *SIAM Journal on control and optimization*, vol. 43, no. 5, pp. 1714–1736, 2005.
- [5] G. Paolo, I. Ferrara, and L. Magni, “MPC for robot manipulators with integral sliding mode generation,” *IEEE/ASME Transactions on Mechatronics*, vol. 22, no. 3, pp. 1299–1307, 2017.
- [6] N. Scianca, D. De Simone, L. Lanari, and G. Oriolo, “MPC for humanoid gait generation: Stability and feasibility,” *IEEE Transactions on Robotics*, vol. 36, no. 4, pp. 1171–1188, 2020.
- [7] R. Grandia, A. J. Taylor, A. Singletary, M. Hutter, and A. D. Ames, “Nonlinear model predictive control of robotic systems with control lyapunov functions,” in *Proceedings of Robotics: Science and Systems*, 2022.

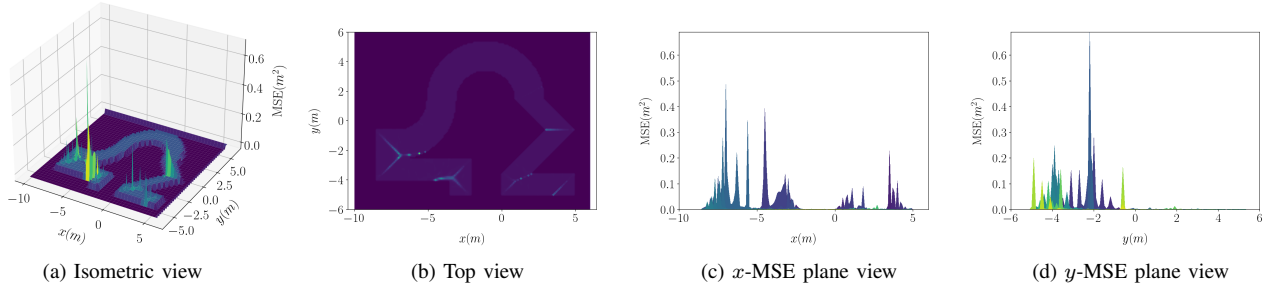


Fig. 10: 3D visualization of the MSE of the testing data.  $x$  and  $y$  represent the positions of the testing points, while MSE represents the prediction error corresponding to the point  $(x, y)$ . The maximum MSE is 0.690 at  $(-5.5, -2.1)$ .

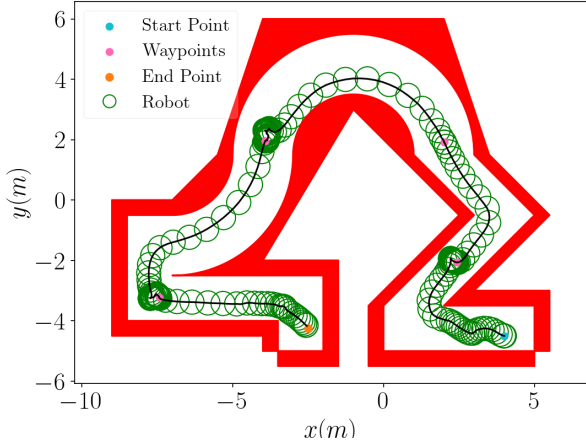


Fig. 11: Five connected closed-loop trajectories, where the start point of each subsequent trajectory is the end point of the previous one, controlled by iMPC-DHOCBF with  $m_{cbf} = 1$ ,  $N = 24$ ,  $\gamma_1 = 0.1$ . Waypoints are manually chosen. The free track is enclosed by two red obstacles. The proposed method works well for safety-critical navigation in narrow space and the animation video can be found at <https://youtu.be/4t8TQ7gJUS8>.

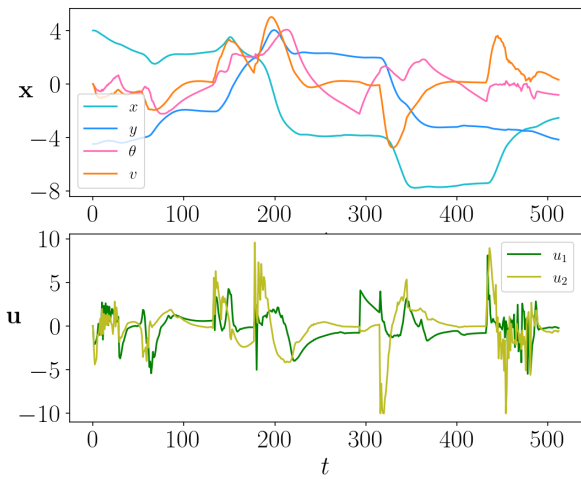


Fig. 12: States and control inputs vary over time steps. These system variables are relative to the motion of the robot shown in Fig. 11 and are subject to the constraints (27).

- [8] T. D. Son and Q. Nguyen, "Safety-critical control for non-affine nonlinear systems with application on autonomous vehicle," in *2019 IEEE 58th Conference on Decision and Control (CDC)*, 2019, pp. 7623–7628.
- [9] J. M. Eklund, J. Sprinkle, and S. S. Sastry, "Switched and symmetric pursuit/evasion games using online model predictive control with application to autonomous aircraft," *IEEE Transactions on Control Systems Technology*, vol. 20, no. 3, pp. 604–620, 2012.
- [10] J. V. Frasch, A. Gray, M. Zanon, H. J. Ferreau, S. Sager, F. Borrelli, and M. Diehl, "An auto-generated nonlinear MPC algorithm for real-time obstacle avoidance of ground vehicles," in *2013 European Control Conference (ECC)*, 2013, pp. 4136–4141.
- [11] A. Liniger, A. Domahidi, and M. Morari, "Optimization-based autonomous racing of 1: 43 scale rc cars," *Optimal Control Applications and Methods*, vol. 36, no. 5, pp. 628–647, 2015.
- [12] X. Zhang, A. Liniger, and F. Borrelli, "Optimization-based collision avoidance," *IEEE Transactions on Control Systems Technology*, vol. 29, no. 3, pp. 972–983, 2020.
- [13] K. Galloway, K. Sreenath, A. D. Ames, and J. W. Grizzle, "Torque saturation in bipedal robotic walking through control lyapunov function-based quadratic programs," *IEEE Access*, vol. 3, pp. 323–332, 2015.
- [14] A. D. Ames, S. Coogan, M. Egerstedt, G. Notomista, K. Sreenath, and P. Tabuada, "Control barrier functions: Theory and applications," in *2019 18th European Control Conference (ECC)*, 2019, pp. 3420–3431.
- [15] Q. Nguyen, A. Hereid, J. W. Grizzle, A. D. Ames, and K. Sreenath, "3d dynamic walking on stepping stones with control barrier functions," in *2016 IEEE 55th Conference on Decision and Control (CDC)*, 2016, pp. 827–834.
- [16] Q. Nguyen and K. Sreenath, "Exponential control barrier functions for enforcing high relative-degree safety-critical constraints," in *2016 American Control Conference (ACC)*, 2016, pp. 322–328.
- [17] W. Xiao and C. Belta, "High-order control barrier functions," *IEEE Transactions on Automatic Control*, vol. 67, no. 7, pp. 3655–3662, 2022.
- [18] X. Tan, W. S. Cortez, and D. V. Dimarogonas, "High-order barrier functions: Robustness, safety, and performance-critical control," *IEEE Transactions on Automatic Control*, vol. 67, no. 6, pp. 3021–3028, 2021.
- [19] J. Usevitch and D. Panagou, "Adversarial resilience for sampled-data systems under high-relative-degree safety constraints," *IEEE Transactions on Automatic Control*, pp. 1–1, 2022.
- [20] W. Xiao, C. Belta, and C. G. Cassandras, "Adaptive control barrier functions," *IEEE Transactions on Automatic Control*, vol. 67, no. 5, pp. 2267–2281, 2021.
- [21] S. Liu, W. Xiao, and C. A. Belta, "Auxiliary-variable adaptive control barrier functions for safety critical systems," in *2023 62nd IEEE Conference on Decision and Control (CDC)*, 2023, pp. 8602–8607.
- [22] Q. Nguyen and K. Sreenath, "Optimal robust control for bipedal robots through control lyapunov function based quadratic programs," in *Robotics: Science and Systems (RSS)*, Rome, Italy, July 2015.
- [23] M. Jankovic, "Robust control barrier functions for constrained stabilization of nonlinear systems," *Automatica*, vol. 96, pp. 359–367, 2018.
- [24] A. Clark, "Control barrier functions for stochastic systems," *Automatica*, vol. 130, p. 109688, 2021.
- [25] S. Liu, W. Xiao, and C. A. Belta, "Feasibility-guaranteed safety-critical control with applications to heterogeneous platoons," *arXiv preprint arXiv:2310.00238*, 2023.

- [26] A. Agrawal and K. Sreenath, "Discrete control barrier functions for safety-critical control of discrete systems with application to bipedal robot navigation." in *Robotics: Science and Systems*, vol. 13. Cambridge, MA, USA, 2017.
- [27] H. Ma, X. Zhang, S. E. Li, Z. Lin, Y. Lyu, and S. Zheng, "Feasibility enhancement of constrained receding horizon control using generalized control barrier function," in *2021 4th IEEE International Conference on Industrial Cyber-Physical Systems (ICPS)*, 2021, pp. 551–557.
- [28] Y. Xiong, D.-H. Zhai, M. Tavakoli, and Y. Xia, "Discrete-time control barrier function: High-order case and adaptive case," *IEEE Transactions on Cybernetics*, pp. 1–9, 2022.
- [29] S. He, J. Zeng, and K. Sreenath, "Autonomous racing with multiple vehicles using a parallelized optimization with safety guarantee using control barrier functions," in *2022 International Conference on Robotics and Automation (ICRA)*, 2022, pp. 3444–3451.
- [30] Z. Li, J. Zeng, A. Thirugnanam, and K. Sreenath, "Bridging model-based safety and model-free reinforcement learning through system identification of low dimensional linear models," in *Proceedings of Robotics: Science and Systems*, 2022.
- [31] J. Zeng, B. Zhang, Z. Li, and K. Sreenath, "Safety-critical control using optimal-decay control barrier function with guaranteed point-wise feasibility," in *2021 American Control Conference (ACC)*, 2021, pp. 3856–3863.
- [32] J. Zeng, Z. Li, and K. Sreenath, "Enhancing feasibility and safety of nonlinear model predictive control with discrete-time control barrier functions," in *2021 60th IEEE Conference on Decision and Control (CDC)*, 2021, pp. 6137–6144.
- [33] M. Srinivasan, A. Dabholkar, S. Coogan, and P. A. Vela, "Synthesis of control barrier functions using a supervised machine learning approach," in *2020 IEEE/RSSJ International Conference on Intelligent Robots and Systems (IROS)*, 2020, pp. 7139–7145.
- [34] M. Saveriano and D. Lee, "Learning barrier functions for constrained motion planning with dynamical systems," in *2019 IEEE/RSSJ International Conference on Intelligent Robots and Systems (IROS)*, 2019, pp. 112–119.
- [35] C. Peng, O. Donca, G. Castillo, and A. Hereid, "Safe bipedal path planning via control barrier functions for polynomial shape obstacles estimated using logistic regression," in *2023 IEEE International Conference on Robotics and Automation (ICRA)*, 2023, pp. 3649–3655.
- [36] A. Robey, H. Hu, L. Lindemann, H. Zhang, D. V. Dimarogonas, S. Tu, and N. Matni, "Learning control barrier functions from expert demonstrations," in *2020 59th IEEE Conference on Decision and Control (CDC)*, 2020, pp. 3717–3724.
- [37] W. Lavanakul, J. Choi, K. Sreenath, and C. Tomlin, "Safety filters for black-box dynamical systems by learning discriminating hyperplanes," in *6th Annual Learning for Dynamics & Control Conference*. PMLR, 2024, pp. 1278–1291.
- [38] S. Liu, J. Zeng, K. Sreenath, and C. A. Belta, "Iterative convex optimization for model predictive control with discrete-time high-order control barrier functions," in *2023 American Control Conference (ACC)*, 2023, pp. 3368–3375.
- [39] M. Sun and D. Wang, "Initial shift issues on discrete-time iterative learning control with system relative degree," *IEEE Transactions on Automatic Control*, vol. 48, no. 1, pp. 144–148, 2003.
- [40] A. Thirugnanam, J. Zeng, and K. Sreenath, "Duality-based convex optimization for real-time obstacle avoidance between polytopes with control barrier functions," in *2022 American Control Conference (ACC)*, 2022, pp. 2239–2246.
- [41] M. A. Kramer, "Autoassociative neural networks," *Computers & chemical engineering*, vol. 16, no. 4, pp. 313–328, 1992.
- [42] B. Stellato, G. Banjac, P. Goulart, A. Bemporad, and S. Boyd, "Osqp: An operator splitting solver for quadratic programs," *Mathematical Programming Computation*, vol. 12, no. 4, pp. 637–672, 2020.
- [43] L. T. Biegler and V. M. Zavala, "Large-scale nonlinear programming using ipopt: An integrating framework for enterprise-wide dynamic optimization," *Computers & Chemical Engineering*, vol. 33, no. 3, pp. 575–582, 2009.

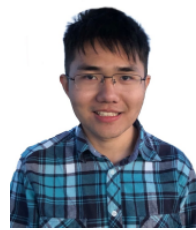
- [44] J. Lofberg, "Yalmip: A toolbox for modeling and optimization in matlab," in *2004 IEEE international conference on robotics and automation (IEEE Cat. No. 04CH37508)*, 2004, pp. 284–289.



**Shuo Liu** received his M.S. degree in Mechanical Engineering from Columbia University, New York, NY, USA, in 2020 and B.Eng. degree in Mechanical Engineering from Chongqing University, Chongqing, China, in 2018. He is currently a Ph.D. candidate in Mechanical Engineering at Boston University, Boston, USA and his research interests include optimization, non-linear control, deep learning and robotics.



**Zhe Huang** received his M.S. degree in Robotics from Boston University, Boston, USA, in 2023 and an M.S. degree in Computer Science from the University of Dayton, Dayton, USA, in 2017. He earned his B.S. degree in Electro-Optics from Jianghan University, Wuhan, China, in 2014. His research interests include deep learning, computer vision, robot perception and robot control.



**Jun Zeng** received his Ph.D. in Control and Robotics from the Department of Mechanical Engineering at the University of California, Berkeley, USA, in 2022, his Dipl. Ing. degree from École Polytechnique, France, in 2017, and his B.S.E. degree from Shanghai Jiao Tong University, China, in 2016. His research interests lie at the intersection of optimization, control, planning, and learning, with applications to various

robotics platforms.



2017. His research interests include the intersection of highly dynamic robotics and applied nonlinear control.

**Koushil Sreenath** received the M.S. degree in Applied Mathematics and the Ph.D. degree in Electrical Engineering and Systems from the University of Michigan, Ann Arbor, MI, USA, in 2011. He is an Assistant Professor of Mechanical Engineering with the University of California, Berkeley, Berkeley, CA, USA. He was an Assistant Professor with Carnegie Mellon University, Pittsburgh, PA, USA, between 2013 and



synthesis and verification, and applications in robotics and biology.

**Calin Belta** received his PhD in Mechanical Engineering from the University of Pennsylvania, Philadelphia, PA, USA, in 2003. He is currently the Brendan Iribe Endowed Professor of Electrical and Computer Engineering and Computer Science at the University of Maryland, College Park, MD, USA. His research focuses on control theory and formal methods, with particular emphasis on hybrid and cyber-physical systems,